

# Performing Bayesian analyses with AZURE2 using BRICK: an application to the <sup>7</sup>Be system

Daniel Odell  $^{1,*}$ , Carl R. Brune  $^1$ , Daniel R. Phillips  $^1$ , Richard James deBoer  $^2$  and Som Nath Paneru  $^{1,3}$ 

- <sup>1</sup>Institute of Nuclear and Particle Physics and Department of Physics and Astronomy, Ohio University, Athens, Ohio 45701, USA
- <sup>2</sup>Department of Physics and the Joint Institute for Nuclear Astrophysics, University of Notre Dame, Notre Dame, Indiana 46556 USA
- <sup>3</sup> Facility for Rare Isotope Beams, Michigan State University, East Lansing, Michigan, USA (present)

Correspondence\*: Daniel Odell dodell@ohio.edu

#### 2 ABSTRACT

- Phenomenological R-matrix has been a standard framework for the evaluation of resolved 3 resonance cross section data in nuclear physics for many years. It is a powerful method for comparing different types of experimental nuclear data and combining the results of many different experimental measurements in order to gain a better estimation of the true underlying cross sections. Yet a practical challenge has always been the estimation of the uncertainty on both the cross sections at the energies of interest and the fit parameters, which can take the form of standard level parameters. Frequentist ( $\chi^2$ -based) estimation has been the norm. In this work, a Markov Chain Monte Carlo sampler, emcee, has been implemented for the R-matrix code AZURE2, creating the Bayesian R-matrix Inference Code Kit (BRICK). Bayesian uncertainty estimation has then been carried out for a simultaneous R-matrix fit of the  ${}^{3}\text{He}(\alpha,\gamma){}^{7}\text{Be}$  and 12  $^3$ He $(\alpha,\alpha)^3$ He reactions in order to gain further insight into the fitting of capture and scattering data. Both data sets constrain the values of the bound state  $\alpha$ -particle asymptotic normalization coefficients in <sup>7</sup>Be. The analysis highlights the need for low-energy scattering data with welldocumented uncertainty information and shows how misleading results can be obtained in its absence.
- 18 Keywords: keyword, keyword, keyword, keyword, keyword, keyword, keyword

#### 1 INTRODUCTION

- 19 Phenomenological R-matrix has been the standard analysis tool for cross section data that exhibit
- 20 overlapping yet resolved resonances for many years (Lane and Thomas, 1958). It is used extensively
- 21 to evaluate data for applications (e.g. the ENDF/B-VIII.0 evaluation (Brown et al., 2018)), to perform
- 22 extrapolations to low, unobserved energies in nuclear astrophysics (e.g. Azuma et al. (2010); Descouvement
- et al. (2005)), and to extract level parameters for nuclear structure (ENSDF, 2022). In all cases, it provides
- 24 a reaction framework in which experimental information of various different types can be combined to

25 improve estimates of the true cross sections. One challenging aspect of this type of analysis has been 26 reliable uncertainty propagation.

Traditionally, data have been fitted using  $\chi^2$  minimization, with uncertainties being estimated using one of two methods. The first is using partial derivatives and the assumption that the quantity of interest is related linearly with the parameters of the model. The second is the assignment of confidence intervals based on some  $\Delta\chi^2$  value. The assumption of linearity is often a poor one and the second method can become tedious or impossible to implement for a complicated model. Additional limitations are that one must assume Gaussian uncertainties on the input data and there is almost no ability to include prior information about the parameters. It is known that  $\chi^2$  methods may lead to biased results and/or underestimated uncertainties in data evaluations (Smith et al.) [2007). The reason for these issues is understood to be incomplete documentation or modeling of systematic uncertainties. While systematic uncertainties are a difficult subject in any approach, they are much easier to model and implement using the Bayesian methods described below. Finally, we would like to point out that a mixed approach is possible, where  $\chi^2$  minimization is combined with a Monte Carlo simulation of some uncertainties. This method was used by deBoer et al.  $|\langle 2014 \rangle\rangle$  in a previous analysis of  $^3\text{He}(\alpha, \gamma)^7\text{Be}$  and  $^3\text{He}(\alpha, \alpha)^3\text{He}$ .

Bayesian methods are increasingly becoming the standard for performing Uncertainty Quantification in physical sciences and engineering in general, and theoretical nuclear physics in particular (Schindler and Phillips, 2009; Furnstahl et al., 2015a,b; Zhang et al., 2015; Melendez et al., 2017; Wesolowski et al., 2019; Neufcourt et al., 2020a, 2019; King et al., 2019; Melendez et al., 2019; Filin et al., 2020; Drischler et al., 2020a, Filin et al., 2021; Schunck et al., 2020; Filin et al., 2021; Schunck et al., 2020; Neufcourt et al., 2020b; Everett et al., 2021; Catacora-Rios et al., 2021; Reinert et al., 2021; Phillips et al., [2021]; [Wesolowski et al., 2021]; [Schnabel et al., 2021]; [Xu et al., 2021]; [Cao et al., 2021]; [Hamaker et al., 2021]). In contrast to a traditional  $\chi^2$ -minimization they offer the opportunity to examine the entire probability distribution for parameters of interest, rather than focusing on the values that maximize the likelihood. Perhaps equally important, in a Bayesian approach it is straightforward—mandatory even—to declare and include prior information on the parameters of interest. Bayesian methods, combined with the possibility to use Markov Chain Monte Carlo sampling to explore a high-dimensional parameter space, allow one to introduce additional parameters without fear of computational instabilities caused by shallow  $\chi^2$  minima. The use of MCMC sampling also makes uncertainty propagation straightforward, as we will demonstrate here. And a Bayesian framework is—to our knowledge—the only option if one wishes to incorporate a rigorous formulation of theory uncertainties into the statistical analysis. In this work, Bayesian uncertainty quantification is implemented by pairing the R-matrix code AZURE2 (Azuma et al., 2010; Uberseder and deBoer, 2015) with the MCMC Python package emcee (Foreman-Mackey et al., 2013). The pairing is facilitated by a Python interface BRICK (Bayesian R-matrix Inference Code Kit), enabling Bayesian inference in the context of R-matrix analyses. 

To benchmark this code, it has been applied to the analysis of the  ${}^{3}\text{He}(\alpha,\gamma){}^{7}\text{Be}$  and  ${}^{3}\text{He}(\alpha,\alpha){}^{3}\text{He}$  reactions. The  ${}^{3}\text{He}(\alpha,\gamma){}^{7}\text{Be}$  reaction is a key reaction in modeling the neutrino flux coming from our sun (Bahcall and Ulrich, 1988). It also plays a role in Big Bang Nucleosynthesis (BBN) (Cyburt et al., 2016). The reaction cross section is dominated by the direct capture process, but also has significant contributions from broad resonances (see Fig. 1). In recent years, high-precision measurements of this reaction have been performed, using direct  $\gamma$ -ray detection (Kontos et al., 2013; Brown et al., 2007; Costantini et al., 2008), the activation method (Singh et al., 2004; Brown et al., 2007; Carmona-Gallardo et al., 2012; Costantini et al., 2008; Bordeanu et al., 2013), and a recoil separator (Di Leva et al., 2009). Additional higher energy measurements have also been made recently by Szücs et al. (2019), but are outside the energy range of the

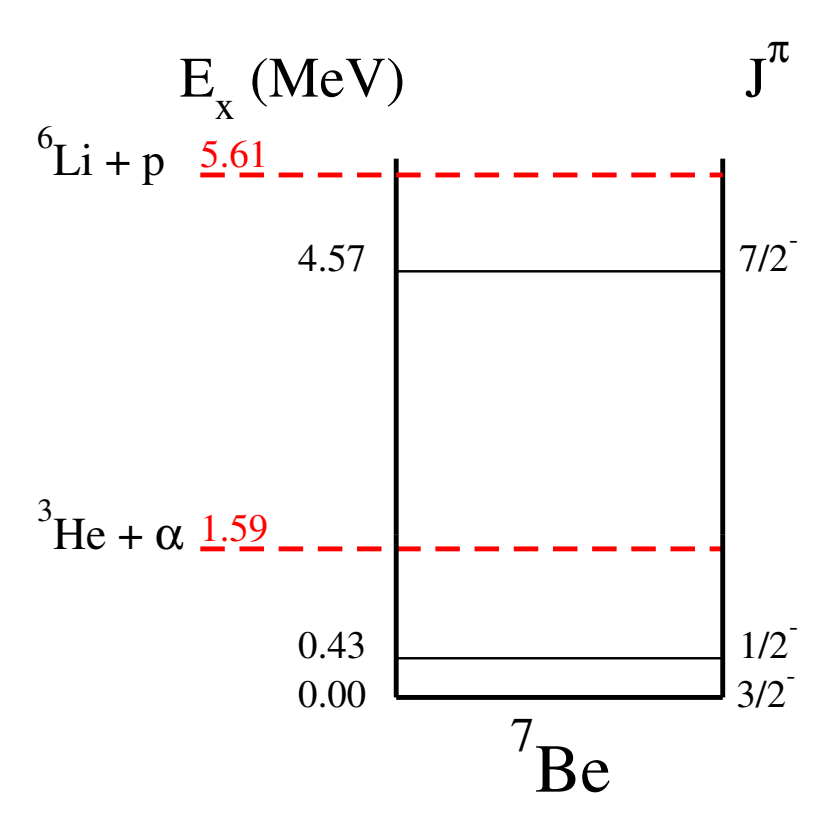


**Figure 1.** Level diagram of <sup>7</sup>Be up to the proton separation energy.

present analysis. Using these high precision measurements, several analyses have been made to combine these data sets and extrapolate the cross section to low energies using pure external capture (Adelberger et al., 2011), *R*-matrix (deBoer et al., 2014), effective field theory (Zhang et al., 2020); Premarathna and Rupak, 2020b), a modified potential model (Tursunov et al., 2021), and *ab initio* calculations (Nollett, 2001); Neff, 2011; Dohet-Eraly et al., 2016; Vorabbi et al., 2019). These several recent analyses make this reaction an ideal case for benchmarking since they employ both more traditional and Bayesian uncertainty estimation methods.

As the energies pertinent to solar fusion and BBN the  ${}^{3}\text{He}(\alpha,\gamma){}^{7}\text{Be}$  cross section has a large contribution from external capture,  ${}^{3}\text{He}(\alpha,\alpha){}^{3}\text{He}$  data, through its constraints on the scattering phase shifts, should also provide an additional source of constraint on the low-energy extrapolation. This type of combined analysis has been reported in deBoer et al. (2014), but there it was found that the available scattering data of Barnard et al. (1964) was inconsistent with the capture data, perhaps because of incomplete uncertainty documentation in the former. With this in mind, new measurements of the  ${}^{3}\text{He}(\alpha,\alpha){}^{3}\text{He}$  cross section were recently reported by Paneru et al. (2022).

In this work, a Bayesian uncertainty analysis is performed on an R-matrix fit to the low energy  ${}^3\text{He}(\alpha,\gamma){}^7\text{Be}$  (Kontos et al., 2013; Costantini et al., 2008; Brown et al., 2007; Singh et al., 2004; Bordeanu et al., 2013; Di Leva et al., 2009) and  ${}^3\text{He}(\alpha,\alpha){}^3\text{He}$  (Barnard et al., 1964; Paneru et al., 2022) data. The Paneru et al. (2022) data is a new measurement performed with the Scattering of Nuclei in Inverse Kinematics (SONIK) detector. The sensitivity of the fit to the scattering data is the main focus, examining the differences resulting from the two different scattering data sets considered. The mapping of the posterior distributions of the fit parameters, cross sections, phase shifts, and scattering lengths gives new insights into the dependence of these quantities to the input scattering data.

#### WHAT IS BRICK?

- BRICK is a python package that acts as an interface between the AZURE2 (Azuma et al., 2010); Uberseder
- and deBoer, (2015) R-matrix code and an MCMC sampler. It is not a replacement for AZURE2 nor is it
- 93 intended to be. The primary functionality that it provides is a user-friendly way to sample parameters that
- have already been set up with the AZURE2 graphical user interface (GUI) to be varied.

#### 2.1 AZURE2 95

- AZURE2 is a multilevel, multichannel, R-matrix code (open source) that was developed under the Joint 96
- Institute for Nuclear Astrophysics (JINA) (Azuma et al., 2010; Uberseder and deBoer, 2015). While 97
- the code was created primarily to handle the added complexity of charged-particle induced capture 98
- reactions (deBoer et al., 2017), also has capability for a wide range of other types of reaction calculations. 99
- The code is primarily designed to be used by way of a GUI, but can also be executed in a command line 100
- mode for batch processes (Uberseder and deBoer, 2015). The code stores all of its setup information in a 101
- simple text input file. While this file is usually edited by way of the GUI, it can also be modified directly. 102
- This may be desirable for batch type calculations, as are being used here. 103
- AZURE2 primarily uses the alternative R-matrix parameterization of Brune (2002). It has two main 104
- advantages. The first is that it eliminates the need for the boundary conditions present in the classical 105
- formalism of Lane and Thomas (1958). The second is that the remaining fit parameters become the observed 106
- level parameters. The remaining model parameters are the channel radii which are fixed at 4.2 fm in this 107
- analysis. 108
- A key advantage in using the parameterization of Brune (2002) for the fitting of low energy capture 109
- reactions is that level parameters for bound or near threshold resonances can be more directly included in 110
- the R-matrix analysis (Mukhamedzhanov and Tribble, 1999; Mukhamedzhanov et al., 2001). The use of 111
- the Bayesian uncertainty estimation further facilitates the inclusion of uncertainty information for these 112
- parameters. This provides an improved method for communicating the level structure information gained 113
- from transfer reaction studies into an R-matrix analysis in a statistically rigorous way. 114

#### 2.2 Implementation

#### 2.2.1 Overview 116

- The role of BRICK in our R-matrix calculations is to act as a mediator. It maps proposed parameters 117
- both R-matrix parameters and normalization factors from an MCMC sampler to AZURE2 and R-matrix 118
- predictions from AZURE2 back to the sampler. First, it accepts proposed points in parameter space,  $\theta$ , 119
- from the sampler in this analysis we use emcee (Foreman-Mackey et al., 2013) and packages 120
- them into a format that AZURE2 can read. Then it reads the output from AZURE2 and presents it as a list. 121
- Each item of the list contains the predictions,  $\mu(\theta)$ , and data, y and  $\sigma$ , corresponding to a specific output 122
- channel configuration. The likelihood, represented in Fig.  $\boxed{2}$  by  $\mathcal{L}$ , can then be calculated according to 123
- the user's choice; the Gaussian likelihood chosen for this work is given below in Eq. (2). Accompanied 124
- by prior distributions,  $\pi$ , one can readily construct a Bayesian posterior,  $\mathcal{P}$ . Prior distributions chosen in 125
- this analysis are given in Section 3.2. The posterior value, or rather its logarithm  $\ln \mathcal{P}$ , is passed back to 126
- emcee. Finally, based on the  $\ln \mathcal{P}$  value, the MCMC algorithm decides to accept or reject the proposed 127
- point, proposes a new  $\theta$ , and the process repeats. A diagram is provided in Fig. 2 to illustrate the qualitative 128
- functionality of the different software packages. The process described above starts at the orange rectangle 129
- labeled "emcee". 130

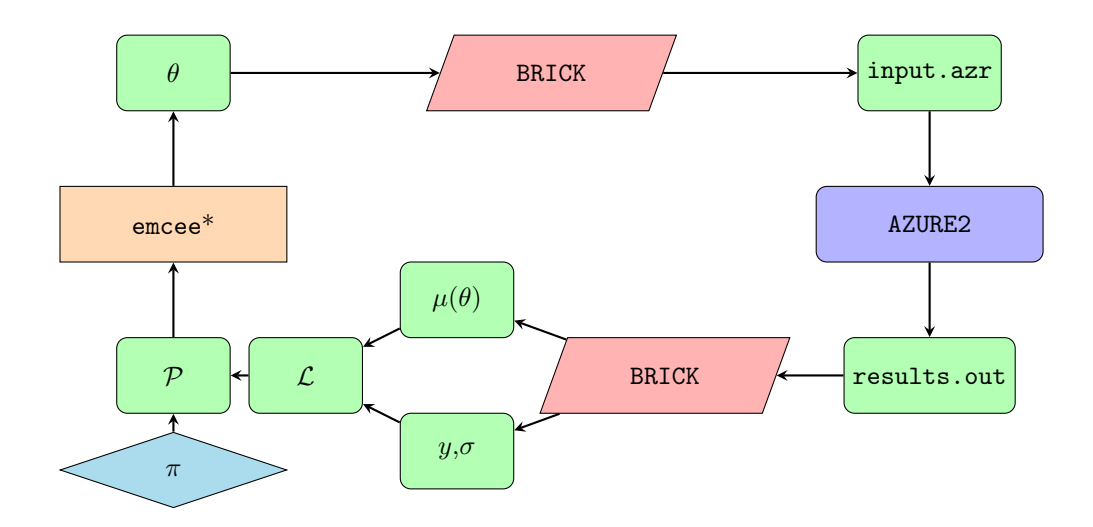


Figure 2. Representation of the different roles of emcee, BRICK, and AZURE2 in the Bayesian analysis presented below. The asterisk in the emcee rectangle indicates the starting point of the process.

#### 2.2.2 Details 131

134

135

136

137

138

140

141

142

143

144

145

146

147

148

149

150

151

152

153

154

155

156

157

BRICK is built such that different samplers can be used. The analysis presented in this paper uses emcee, 132 so the details provided in this section will be somewhat specific to it. 133

When initializing an instance of an EnsembleSampler, the most relevant argument is log\_prob\_fn, the function that returns the logarithm of the probability. One of the advantages of emcee is that it allows the practitioner to perform arbitrary calculations inside that probability function. That function must meet only two requirements: (1) take an array of floating point numbers that represents the vector in parameter space and (2) return a floating point number that represents the logarithm of the probability associated with that array. In between those two steps, one is free to perform whatever calculations one needs. This can be 139 seen on the left-hand side of Fig. 2. The parameter-space vector,  $\theta$ , is output from emcee. The logarithm of the probability at that point,  $\ln \mathcal{P}$ , is subsequently input to emcee. In this sense, emcee is well-suited to the implementation of "black-box" physics models where one has limited access to the source code.

The primary tasks that BRICK accomplishes are (1) translating  $\theta$  into a format that AZURE2 can read and (2) reading the output from AZURE2 such that a  $\ln \mathcal{P}$  value can be easily calculated. The means of accomplishing these tasks relies on the command-line interface (CLI) to AZURE2, which is accessible when installed on Linux machines. The CLI options available to AZURE2 are well documented in the manual (Uberseder and deBoer, 2015). The most critical argument is the input file, typically accompanied by the file extension .azr. This input file contains all of the necessary information to perform an R-matrix calculation with a given set of parameters. It is generated when the R-matrix and data models are built with the commonly used GUI, which AZURE2 provides. BRICK is not built to replace that GUI. It accompanies AZURE2 by allowing the user to bring their AZURE2-prepared R-matrix model over and sample what was previously optimized. Accordingly, the default behavior of BRICK is to respect the choices made by the user in the AZURE2 GUI. If a parameter is fixed in AZURE2, it is fixed in BRICK. If it is varied in AZURE2, it is sampled in BRICK.

BRICK accesses the AZURE2 CLI through the Python module subprocess. But prior to that, BRICK must map the values in  $\theta$  to the proper locations in the input file. This is accomplished by reading the <levels> and <sectionsData> sections of the input file. BRICK reads the appropriate parameters

168

169 170

171172

173

174

188

189

190

191

192

193

194

195 196

and flags looking for varied parameters. As they are found, their locations are stored. When a new  $\theta$  is proposed, BRICK creates a new input file and maps the values in  $\theta$  to the varied parameter locations. Then AZURE2 is called with the newly generated input file. The output from AZURE2 is written to a sequence of files in the output directory by default. Those files are read and the predictions,  $\mu$ , and experimental data, y, are extracted. A likelihood is then constructed. Under the assumption that the uncertainties associated with y are uncorrelated and normally distributed, this is a multivariate Gaussian distribution. Accompanied by a list of prior distributions corresponding to the preexisting knowledge of the sampled parameters, a posterior is finally constructed and passed back to emcee.

Initially, this process was built in a single-threaded manner. As emcee is a ensemble sampler, efficient exploration of the posterior relies heavily on many, simultaneous walkers. In order to scale this beyond the most basic calculations, we modified our implementation to allow each walker to write its own input file and read from its own output directory. Inside the log-probability function, there is no access to any kind of walker identifier, so each walker generates a file-space that is uniquely identified by an eight-character random string. This allows each walker to work independently, so on systems where many cores are available, each walker can have a dedicated core. Or at least the time spent waiting for CPU time is minimized. This also allows for an increased number of walkers, which is a common tactic used to decrease autocorrelation time.

## 3 APPLICATION TO ${}^{3}\text{He}(\alpha,\alpha){}^{3}\text{He AND }{}^{3}\text{He}(\alpha,\gamma){}^{7}\text{Be}$

#### 175 3.1 The R-matrix model

The starting point for the R-matrix model used here was that of deBoer et al. (2014). In that work, ten 176 levels were used with three particle pairs ( ${}^{3}\text{He}+\alpha$ ,  ${}^{7}\text{Be}+\gamma_{0}$ , and  ${}^{7}\text{Be}+\gamma_{1}$ ) for a total of 16 R-matrix fit 177 parameters. Initial MCMC calculations showed that a 7/2<sup>-</sup> background level used in deBoer et al. (2014) 178 was not statistically significant, and was thus dropped from the calculation. This already demonstrated one 179 of the powerful feature of this type of MCMC analysis, it provided a clear identification of redundant fit 180 parameters. Likewise, we verified that the exact placement of many of the background levels did not effect 181 the fit results, as long as they were placed at sufficiently high energies. The exception to this was the  $5/2^-$ 182 background level, placed at 7 MeV. Because there are two real levels at  $E_x$  = 6.73 and 7.21 MeV in <sup>7</sup>Be, 183 this background level needed to be placed close to their energies. It was found that this single background 184 level was sufficient to model both the contributions from these levels and additional higher energy 5/2 185 186 levels. The R-matrix model used here thus consisted of nine levels, three particle pairs, and 16 R-matrix fit parameters as summarized in Table 11. 187

#### 3.2 Priors on R-matrix parameters

Because this is a Bayesian analysis, we must choose priors for all R-matrix parameters. We have chosen to employ uninformative, uniform priors. However, the signs of the reduced width amplitudes (that is the interference solution), which are implemented in AZURE2 by the signs of the partial widths, were determined by the initial best  $\chi^2$  fit using AZURE2. In this case, a unique interference solution was found. This may not always be the case: sometimes other interference solutions may be possible. The emcee sampler may then not be able to easily find these other interference solutions in the parameter space. It seems to be likely that in cases where different interference solutions are possible, each one will require a separate emcee analysis.

**Table 1.** Sampled parameters in the R-matrix model. Numbers indicate that the level energies were fixed. A distribution indicates that the corresponding parameter was sampled. The subscripts  $\alpha$  and  $\gamma$  indicate the exit particle pair — scattering and capture, respectively. Capture particle pairs are distinguished by ground (0) and excited (1)  $^7\mathrm{Be}$  states. The signs of the partial widths and ANCs indicate the signs of the corresponding reduced width amplitudes. The second column,  $E_{\lambda}$ , is given in excitation energy relative to the ground state.

$J^{\pi}$	$E_{\lambda}$ (MeV)	Widths and ANCs	Prior Distributions
$1/2^{-}$	0.4291	$C_1$	U(1,5 MeV)
$1/2^{-}$	21.6	$\Gamma_{\alpha}$	U(-200, 200 MeV)
$-1/2^{+}$	14	$\Gamma_{lpha} \ \Gamma_{\gamma,0}$	$U(0, 100 \mathrm{MeV})$ $U(0, 10 \mathrm{MeV})$
•		$\Gamma_{\gamma,1}$	U(-10, 10 keV)
$3/2^{-}$	0	$C_0$	U(1,5 MeV)
$3/2^{-}$	21.6	$\Gamma_{\alpha}$	U(-100, 100 MeV)
3/2+	12	$\begin{array}{c} \Gamma_{\alpha} \\ \Gamma_{\gamma,0} \\ \Gamma_{\gamma,1} \end{array}$	U(0, 100 MeV) U(-10, 10 keV) U(-3, 3 keV)
$-5/2^{-}$	7	$\Gamma_{\alpha}^{\prime,1}$	U(0, 100 MeV)
5/2+	12	$\Gamma_{lpha} \ \Gamma_{\gamma,0}$	U(0, 100 MeV) U(-100, 100 MeV)
7/2-	U(1, 10 MeV)	$\Gamma_{lpha}$ $\Gamma_{\gamma,0}$	U(0, 10 MeV) U(0, 1 keV)

One common circumstance where a Bayesian analysis will improve on previous uncertainty estimates is in the ability to give priors for bound state level parameters determined from transfer studies. Unfortunately, in the case of the  $^7$ Be system, there is limited information available for the bound state  $\alpha$ -particle ANCs. A recent first measurement has been reported by Kiss et al. (2020), but the ANCs are rather discrepant from those found from this and past R-matrix analyses of capture data. This inconsistency has not been investigated here, but needs to be addressed in future work. If reliable bound-state ANC determinations become available, that are independent of the capture and scattering data, it provides a path to further decrease the uncertainty in the low energy S-factor extrapolation. One could also adopt priors on the ANCs from *ab initio* calculations, although we have not done so.

It is also tempting to implement more constraining priors into the R-matrix analysis from a compilation like the National Nuclear Data Center or the TUNL Nuclear Data Project (Tilley et al.) 2002). However, great care must be taken to understand the source of the values and uncertainties when weighted averages are used to determine adopted values for level parameters in these compilations. In particular, past analysis of the data being fit in the R-matrix analysis may be a contributor to the evaluation values. Thus blindly using evaluation level parameters and uncertainties can lead to double counting and an erroneous decrease of uncertainties. It is for this reason that uniform priors on parameters are adopted in the present analysis. The posterior shapes then clearly stem solely from the data sets considered in the R-matrix analysis.

The priors for the R-matrix parameters used in this work are listed in Table I. In all but one case, level energies are fixed. The exception is the  $7/2^-$  level energy which corresponds to the lowest lying  $7/2^-$  resonance. The lowest  $1/2^-$  and  $3/2^-$  levels and the  $7/2^-$  level are the only levels inside or below the energy range covered by the analyzed data. All other levels are background levels. For more details of the choices made in formation of the R-matrix model, see Paneru (2020). The distribution formed by the

product of these R-matrix priors and priors on the parameters introduced in the next section is the overall prior  $\pi$  shown in Fig. [2].

## 221 3.3 Modeling systematic errors in the data

#### 222 3.3.1 Common-mode errors

AZURE2 provides a method for the inclusion of a common-mode error for each data set using a modified  $\chi^2$  function

$$\chi^2 = \sum_{\alpha=1}^{N_{\text{sets}}} \left( \sum_{j=1}^{N_{\alpha}} \frac{(f(x_{\alpha,j}) - c_{\alpha} n_{\alpha} y_{\alpha,j})^2}{(c_{\alpha} n_{\alpha} \sigma_{\alpha,j})^2} + \frac{((c_{\alpha} - n_{\alpha})/n_{\alpha})^2}{\delta_{c_{exp},\alpha}^2} \right), \tag{1}$$

where  $c_{\alpha}$  is the normalization fit parameter,  $n_{\alpha}$  is the starting normalization which is set to 1 in the present analysis,  $f(x_{\alpha,j})$  is the differential scattering cross section form the R-matrix,  $y_{\alpha,j}$  is the data point value,  $\sigma_{\alpha,j}$  is the combined statistical and point-to-point uncertainty of a data point, and  $\delta_{c_{exp},\alpha}$  is the fractional common-mode uncertainty of the data set. The additional term in the  $\chi^2$  function is derived by making the approximation that the common-mode systematic uncertainty has a Gaussian probability distribution (D'Agostini, 1994). The accuracy of this approximation is often unclear (Smith et al., 2007).

Common-mode errors are implemented in the present analysis in BRICK, outside of AZURE2, i.e., the common-mode errors are applied to the AZURE2 output. In BRICK the R-matrix parameter set  $\theta_R$  is augmented by a set of normalization factors  $f_{\alpha}$  and energy shifts,  $\Delta_{E,\alpha}$ . (At present energy shifts are only implemented for scattering data.) The overall parameter set  $\theta$  is then the union of the set  $\theta_R$  and  $\{f_{\alpha}, \Delta_{E,\alpha}\}$ . The likelihood  $\mathcal L$  is formed as a product of standard Gaussian likelihoods for each data point, but with normalization factors applied to the AZURE2 predictions  $\mu$ :

$$\mathcal{L} \propto \prod_{\alpha=1}^{N_{\text{sets}}} \prod_{j=1}^{N_{\alpha}} \exp\left(-\frac{(y_{j\alpha} - f_{\alpha}\mu(x_{j\alpha}; \theta_R))^2}{2\sigma_{j\alpha}^2}\right),\tag{2}$$

where we have omitted overall factors that do not affect the parameter estimation. Here  $x_{j\alpha}$  represents the kinematics of the jth data point in data set  $\alpha$ . For scattering data sets,  $x_{j\alpha}$  defines the energy and angle at which the measurement was made. In those cases exclusively,  $\Delta_{E,\alpha}$  is added to the energy.  $\sigma_{j\alpha}$  is the combined statistical and point-to-point uncertainty of the corresponding datum,  $y_{j\alpha}$ .  $N_{\alpha}$  is the number of points in data set  $\alpha$ , and the product over  $\alpha$  runs over all the sets that have independent common-mode errors.

The priors on the  $f_{\alpha}$ 's are specified by the BRICK user. If a Gaussian prior centered at 1 with a width equal to the common-mode error reported in the original experimental publication is employed for the  $f_{\alpha}$ 's, then the product of that prior on the normalization factors and the likelihood Eq. (2) has the same maximum value as the "extended likelihood" corresponding to Eq. (1), that is used to estimate the  $f_{\alpha}$ 's in the frequentist framework implemented in AZURE2.

In our analysis of the  ${}^{3}\text{He}(\alpha,\alpha){}^{3}\text{He}$  and  ${}^{3}\text{He}(\alpha,\gamma){}^{7}\text{Be}$  reactions, we adopted such a Gaussian prior, truncated to exclude negative values of the cross section. We used a different  $f_{\alpha}$  for each energy bin in the SONIK data, detailed in Section 4.2, with the widths of the prior given by the common-mode errors stated in Table 2. The common-mode error associated with the Barnard data, described in Section 4.1, is taken to be 5%. The width of the priors for the  $f_{\alpha}$ 's to be applied to the capture data, discussed in Section 4.3, are

Energy (keV/u)	No of Data Points	Common-Mode Errors
239	17	6.4
291	29	7.6
432	45	9.8
586	46	5.7
711	52	4.5
$873^{(1)}$	52	6.2
$873^{(2)}$	52	4.1
1196	52	7.7
1441	53	6.3
1820	53	8.9

**Table 2.** Common-mode errors associated with the SONIK measurements.

Data Set	Total Capture	Branching Ratio	$\delta_{\text{common}}$ (%)
Seattle, (Brown et al., 2018)	8 pts [0.57, 2.17 MeV]	8 pts [0.57, 2.17 MeV]	3
Weizmann, (Singh et al., 2004)	4 pts [0.74, 1.67 MeV]	<u>-</u>	3.7
LUNA, (Costantini et al., 2008)	7 pts [0.16, 0.30 MeV]	3 pts [0.17, 0.30 MeV]	3.2
ERNA, (Di Leva et al., 2009)	47 pts [1.23, 5.49 MeV]	6 pts [1.93, 4.55 MeV]	5
Notre Dame, (Kontos et al., 2013)	17 pts [0.53, 2.55 MeV]	17 pts [0.53, 2.55 MeV]	8
ATOMKI, (Bordeanu et al., 2013)	5 pts [2.58, 4.43 MeV]	-	6

**Table 3.** Details of the capture data considered in this work: number of data points, energy ranges, and common-mode errors ( $\delta_{\text{common}}$ ). Energies are given the laboratory frame.

specified by the common-mode errors listed in Table [3]. All normalization-factor priors are of the form

$$T(0,\infty)N(1,\sigma_{f\alpha}^2)\,, (3)$$

254 where

257258

259

260

261

262

263264

265266

267

268

$$T(a,b) = \begin{cases} 1 & [a,b] \\ 0 & \text{otherwise} \end{cases}, \tag{4}$$

and  $N(\mu, \sigma^2)$  represents a Gaussian distribution centered at  $\mu$  with a variance of  $\sigma^2$ .

#### 256 3.3.2 Energy shifts

BRICK also has the capability of estimating (overall) beam-energy shifts in a particular data set. This is implemented as another parameter to be estimated  $\Delta_{E,\alpha}$ . This parameter affects all the AZURE2 evaluations for data set  $\alpha$ . BRICK implements the energy shift by generating a different input and data files for each value of  $\Delta_{E,\alpha}$  under consideration. The flowchart of Fig. 2 is thus not strictly accurate when this feature is included. Gaussian priors were defined, centered at zero, on possible energy shifts for the SONIK data and the Barnard data. The widths of the priors are based on information in the original papers, as summarized in Sections 4.1 and 4.2 For the SONIK data, the energy-shift parameter's prior has a standard deviation of 3 keV, based on the energy uncertainty quoted in Paneru et al. (2022). Barnard et al. (1964) cites a much larger uncertainty of 20-40 keV, depending upon the energy. The standard deviation of the prior on the  $\Delta E$  parameter is taken to be 40 keV for this data set, a much larger value than for the SONIK data. It should be noted that the energy uncertainty for the Barnard data set is not a constant, but it is not possible to improve our modeling of this uncertainty due to the lack of documentation of its origin.

282

283

284

285

286

287

288

289

290

291

292293

294

295

#### 4 DATA SETS

### 269 4.1 Barnard et al. (1964) ${}^{3}$ He- $\alpha$ elastic scattering

Measurements of the elastic scattering products resulting from a <sup>3</sup>He beam incident on a <sup>4</sup>He target were 270 reported in 1964 by Barnard et al. (1964), for  $2.4 \le E[^3\text{He}, \text{lab}] \le 5.7 \text{ MeV}$  (1.4  $\le E_{\text{c.m.}} \le 3.3 \text{ MeV}$ ). 271 The experiment provides excitation functions of differential cross section at eight center-of-mass (c.m.) 272 angles covering  $31.55^{\circ} \le \theta$  [<sup>3</sup>He, lab]  $\le 91.94^{\circ}$  ( $54.77^{\circ} \le \theta_{\rm c.m.} \le 140.8^{\circ}$ ). The systematic uncertainty 273 in the measurements is estimated to be 5%. Detailed point-to-point uncertainties are not given, but are 274 stated to be about 3%. The measurements are subject to a significant energy uncertainty, estimated to be 275 20 keV below  $E[^3\text{He}, \text{lab}] = 4 \text{ MeV}$  and 40 keV above that energy. It was also noted by the authors that 276 their beam energy was only reproducible to the level of 20 keV. In total, there are 646 data points collected 277 at 577 unique energies. The data were obtained from EXFOR in the fall of 2021 and converted into the 278 laboratory frame when necessary. All eight angles were included. The previous analysis by deBoer et al. 279 (2014) omitted the largest angle. 280

### 4.2 Paneru et al. ${}^{3}$ He- $\alpha$ elastic scattering

A new measurement of  ${}^{3}\text{He}+\alpha$  elastic scattering was performed at TRIUMF using the SONIK (Connolly, 2015; Paneru, 2020) target and detector system. SONIK was filled with  ${}^{4}\text{He}$  gas maintained at a typical pressure of 5 Torr bombarded with  ${}^{3}\text{He}$  with a beam intensity of about  $10^{12}$  pps. Elastic scattering cross sections were measured at nine different energies from  $E_{\text{c.m.}} = 0.38-3.13$  MeV. SONIK covers an angular range of  $30^{\circ} < \theta_{\text{c.m.}} < 139^{\circ}$ —a markedly larger range than previous measurements. The detectors in SONIK were arranged such that they observed three different points, termed interaction regions, in the gas target along the beam direction. When the beam traversed the gas target it lost energy, so the bombarding energy, and therefore the scattering energy, was slightly different in each of the three interaction regions.

As we will explore further below, the results for the differential scattering cross section from this measurement are consistent with previous determinations but have better precision. The data also extend to markedly lower energies. The uncertainties with this measurement are well quantified and are presented in Paneru et al. (2022). A separate normalization uncertainty is determined for each beam energy. These normalization uncertainties range from 4.1-9.8 %.

#### 4.3 ${}^{3}\text{He}(\alpha, \gamma)$ data

The data selection (Kontos et al., 2013; Costantini et al., 2008; Brown et al., 2007; Singh et al., 2004; 296 Bordeanu et al., 2013; Di Leva et al., 2009) for the  ${}^{3}\text{He}(\alpha,\gamma){}^{7}\text{Be}$  reaction for this work follows that 297 of previous recent works (Adelberger et al., 2011; deBoer et al., 2014; Zhang et al., 2020; Cyburt and 298 Davids, 2008). Note that the LUNA measurements of Gyürky et al. (2007) and Confortola et al. (2007) are 299 collected in Costantini et al. (2008). The combined data sets cover a wide energy range from  $E_{\rm c.m.} = 94$ 300 to 3130 keV, but still remain below the proton decay threshold. Older data are not included due to a long 301 history of discrepancies, which manifested as differences between experiments that used either direct 302 detection of  $\gamma$ -rays or the activation technique. More recent measurements have achieved consistency 303 resulting from improved experimental techniques by performing consistency check measurements using 304 both direct detection of  $\gamma$ -rays and the activation technique (Adelberger et al., 2011). Details about the 305 capture data sets, including common-mode errors for cross sections, are listed in Table 3 306

#### 307 4.4 Data Models

- Two distinct data models are analyzed here,  $\mathcal{D}_{CS}$  and  $\mathcal{D}_{CSB}$ , where C indicates the inclusion of the
- capture data described in Sec. 4.3 S indicates the inclusion of the SONIK data described in Sec. 4.2, and B
- indicates the inclusion of the Barnard data described in Sec.  $4.1 \mathcal{D}_{CSB}$  is a more complete data model in
- 311 the sense that it includes more data and would naively be considered the "best" data model. But, there are
- 312 notable effects when the data of Barnard et al. (1964) are included that are highlighted and discussed in
- 313 Section 5

#### 5 RESULTS

- 314 The results of our analysis are presented here in two subsections. The first discusses results in the energy
- 315 regime of the data that was analyzed. The second computes extrapolated quantities observables that lie
- in energy regimes outside those covered by the analyzed data.

#### 317 **5.1 Fits to data**

- 318 First we examine the extent to which our results match experimental data. We do this by comparing
- 319 predicted and measured observables.

#### 320 5.1.1 Capture Data

- Figure  $\boxed{3}$  shows the total capture S-factor data alongside bands representing 68% intervals from the
- 322 analyses of both data models,  $\mathcal{D}_{CSB}$  and  $\mathcal{D}_{CS}$ . For energies above 400 keV both analyses give very similar
- 323 results. However, below that energy, the  $\mathcal{D}_{\mathrm{CS}}$  analysis provides a more "natural" agreement with data —
- 324 see the normalization factor posteriors and the associated discussion below. The LUNA data in particular
- 325 discriminate between the two data models. The fit to the CSB data includes a normalization factor for
- 326 the LUNA data that differs from 1 by about three times the stated common-mode error, cf. below. The
- normalization factors are not applied to the data in Fig. 3, which is why the CSB band sits well below the
- 328 LUNA data.
- 329 The branching ratio, defined as the ratio of the excited-state cross section to the ground-state cross section,
- 330 results for both data models— $\mathcal{D}_{CS}$  and  $\mathcal{D}_{CSB}$ —are shown in Fig. 4. The most prominent differences
- 331 between the  $\mathcal{D}_{CSB}$  and  $\mathcal{D}_{CS}$  results occur near the upper and lower ends of the energy range. However, in
- 332 the context of the experimental uncertainties, these differences are not significant. Over the entire energy
- 333 range, the predictions from  $\mathcal{D}_{CS}$  and  $\mathcal{D}_{CSB}$  overlap at the 1- $\sigma$  level.

#### 334 5.1.2 Scattering Data

- The differential cross sections from the SONIK (Paneru et al., 2022) and Barnard et al. (1964)
- measurements are shown in Figs. 5 and 6, respectively, with the predictions from our analyses. In all cases,
- 337 both analyses reproduce the data to high accuracy. However, the  $\mathcal{D}_{CS}$  analysis results in a much lower
- 338  $\chi^2$ /datum at max ln P: 0.72 for the SONIK (Paneru et al., 2022) data vs. 0.95 for the  $\mathcal{D}_{\text{CSB}}$  analysis of the
- 339 SONIK + Barnard (Barnard et al., 1964) data sets.

#### 340 5.2 Parameter Distributions

- 341 Separate corner plots for each data model are provided in the Supplemental Material. There are notable
- 342 differences in several R-matrix parameters. In particular, the  $\mathcal{D}_{CS}$  ANCs are significantly larger and their

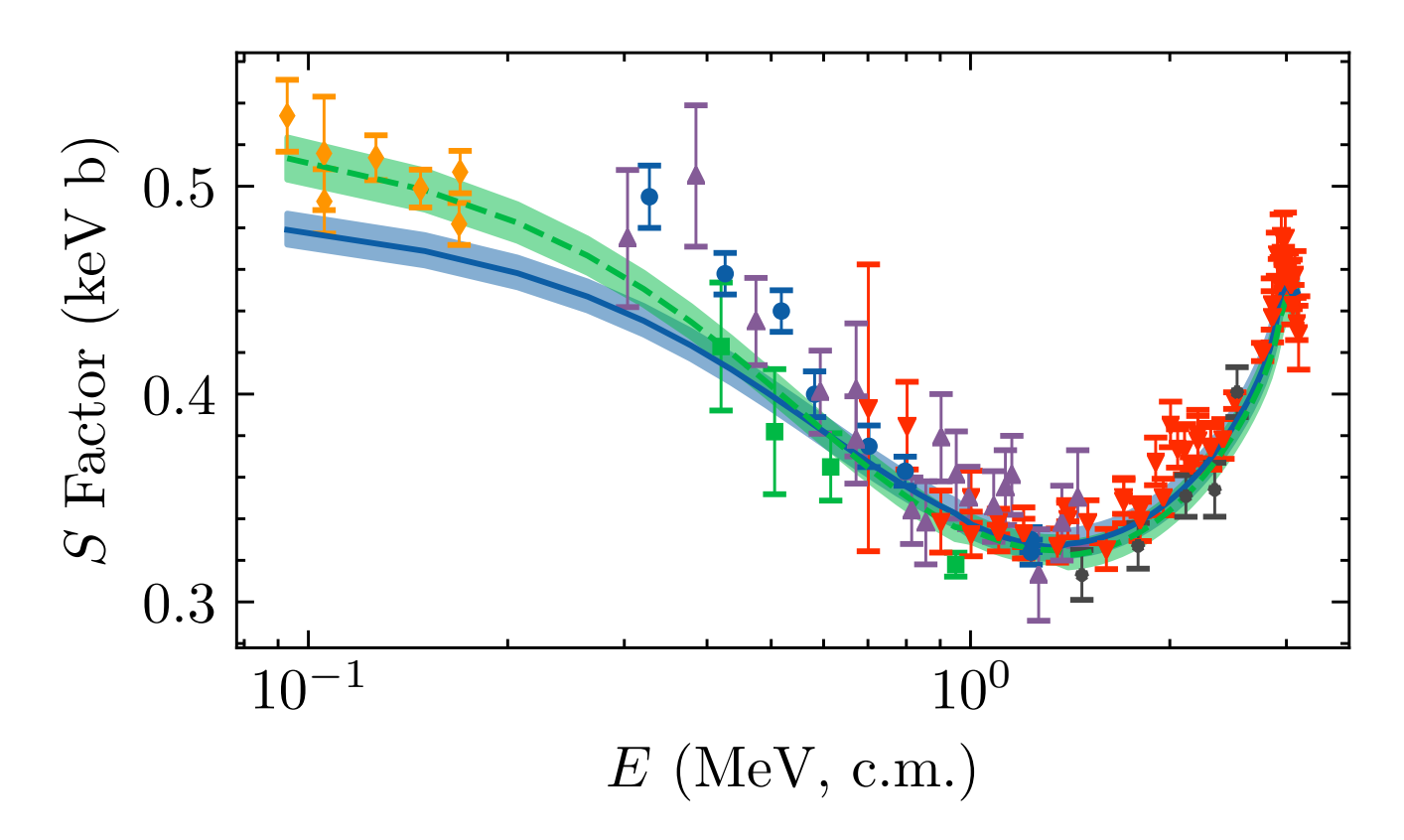
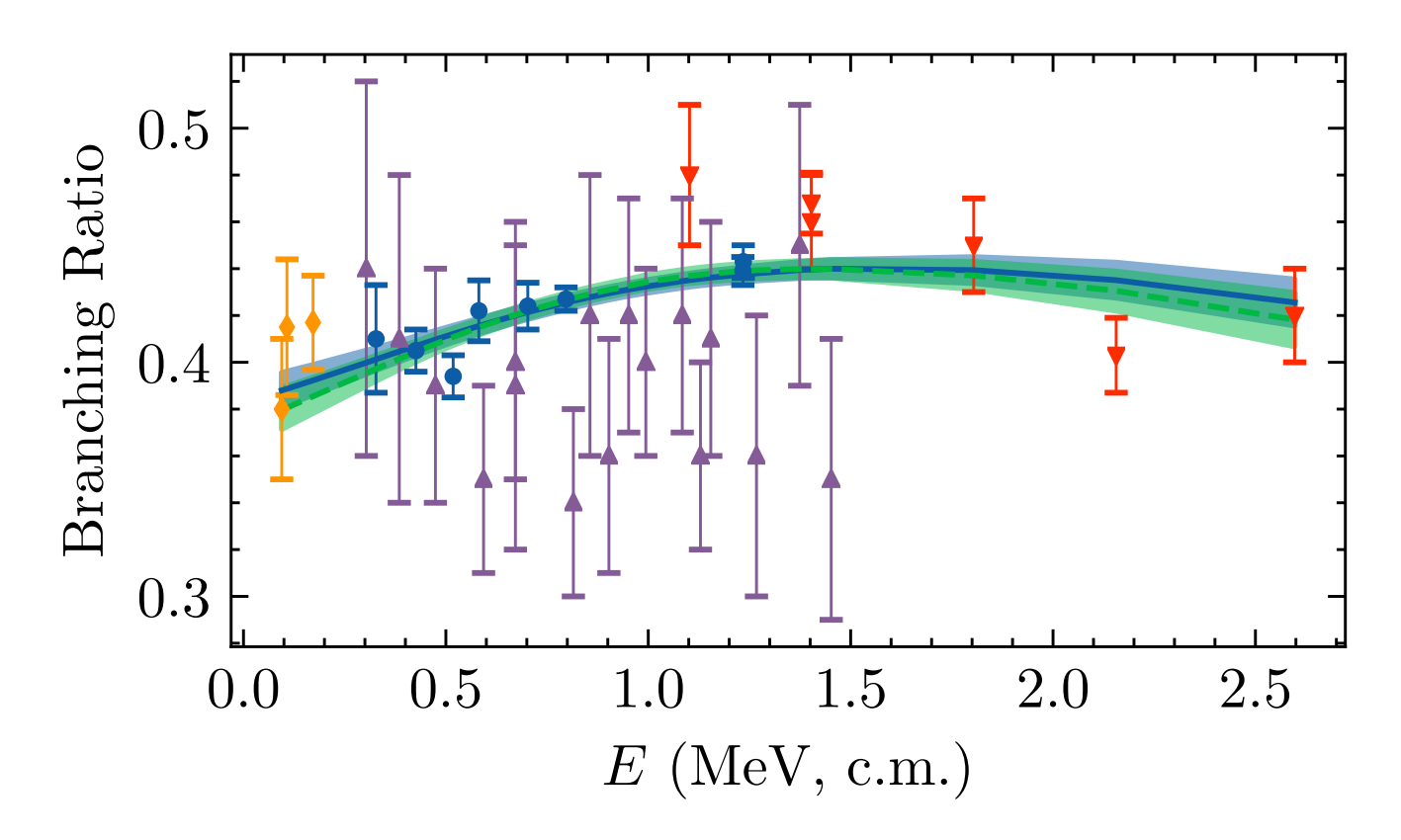


Figure 3. Total capture S factor from Seattle (Brown et al., 2018) (blue circles) Weizmann (Singh et al., 2004) (green squares), LUNA (Costantini et al., 2008) (orange diamonds), ERNA (Di Leva et al., 2009) (red, downward-pointing triangles), Notre Dame (Kontos et al., 2013) (purple, upward-pointing triangles), and ATOMKI (Bordeanu et al., 2013) (black stars) data sets are shown with reported error bars.  $\mathcal{D}_{CSB}$  and  $\mathcal{D}_{CS}$  results are shown with blue and green bands, respectively. The band indicates 68% intervals. The solid, blue line indicates the median prediction from the  $\mathcal{D}_{CSB}$  analysis. The dashed, green line indicates the median prediction from the  $\mathcal{D}_{CS}$  analysis. Normalization factors have not been applied to either the theory prediction or data, so estimates of the extent to which BRICK's fit agrees with the different data sets are not straightforward to make from the figure.

posterior distributions are noticeably wider. The  $\mathcal{D}_{CS}$  analysis also produces a significantly smaller ratio of ANCs,  $C_1/C_0$ . This is consistent with the smaller branching ratios at low energies shown in Fig. [4].

The  $\mathcal{D}_{\mathrm{CS}}$  partial  $\alpha$  widths in the  $1/2^+$ ,  $3/2^+$ , and  $5/2^+$  channels are smaller and separated by more than two standard deviations from the  $\mathcal{D}_{\mathrm{CSB}}$  widths. The distributions for  $\Gamma_{\gamma,0}^{(5/2^+)}$  seem to indicate opposite signs. The  $\mathcal{D}_{\mathrm{CSB}}$   $E_x^{(7/2^-)}$  posterior is markedly smaller and narrower, and the constraints on  $\Gamma_{\alpha}^{(7/2^-)}$  from  $\mathcal{D}_{\mathrm{CSB}}$  are dramatically tighter. This is presumably due to the much larger amount of data in the vicinity of the  $7/2^-$  resonance that is present in the Barnard et al. (1964) data set. It is also worth noting the "non-Gaussian" behavior of several of these distributions—a characteristic that would be difficult to identify in a typical analysis that assumed linear propagation of uncertainties around a minimum of the posterior pdf. Using Gaussian approximations and linearizing would likely underestimate uncertainties in the case of  $\Gamma_{\gamma,0}^{(3/2^+)}$ , for example.

All parameters shown in Fig. 7 are well-constrained. By comparing to the prior distributions listed in Table 1, one can see the dominance of the data's influence over the information in the prior: all



**Figure 4.** The branching ratio predictions are shown alongside the four analyzed branching ratio data sets: Seattle (Brown et al., 2018), LUNA (Costantini et al., 2008), ERNA (Di Leva et al., 2009), and Notre Dame (Kontos et al., 2013). Colors, symbols, and line styles are the same as Fig 3. Bands indicate 68% intervals.

posterior distributions are markedly narrower than the priors chosen. As discussed in Sec. 3.2, several *R*-matrix-model iterations were taken to remove redundant parameters.

The correlation matrix of the R-matrix parameters is shown in Fig.  $\overline{\mathbb{S}}$ . The figure represents an approximation of the full information contained in the corner plot given in the Supplemental Material. There, significant, often-nonlinear, correlations are observable between several pairs of R-matrix parameters. In particular, the influence of the ANCs over the entire R-matrix parameter space, either directly or indirectly, means that it is very important for scattering data to have well-defined uncertainties over its full energy range.

The normalization factors applied to the theory predictions for each of the total capture data sets are shown for both data models in Fig. [9]. The comparison reveals good agreement between  $\mathcal{D}_{CS}$  and  $\mathcal{D}_{CSB}$  for all but the LUNA data set (Costantini et al.), [2008)—the lowest-energy capture data set in our analysis. The  $\mathcal{D}_{CS}$  analysis yields a normalization factor for these data that is very close to 1. In contrast, the  $\mathcal{D}_{CSB}$  analysis requires that the LUNA data be shifted by nearly 10%. (Recall from Eq. (2), that f is applied to the theory prediction, and so an f > 1 corresponds to a systematic error that reduces the experimental cross section and uncertainties.) To put this in perspective, the LUNA collaboration estimates their common-mode error at 3.2%. Because the LUNA data set is the lowest capture data set, this disagreement between the  $\mathcal{D}_{CSB}$  analyses corresponds to a significant difference in the extrapolated S(0) of these two analyses.

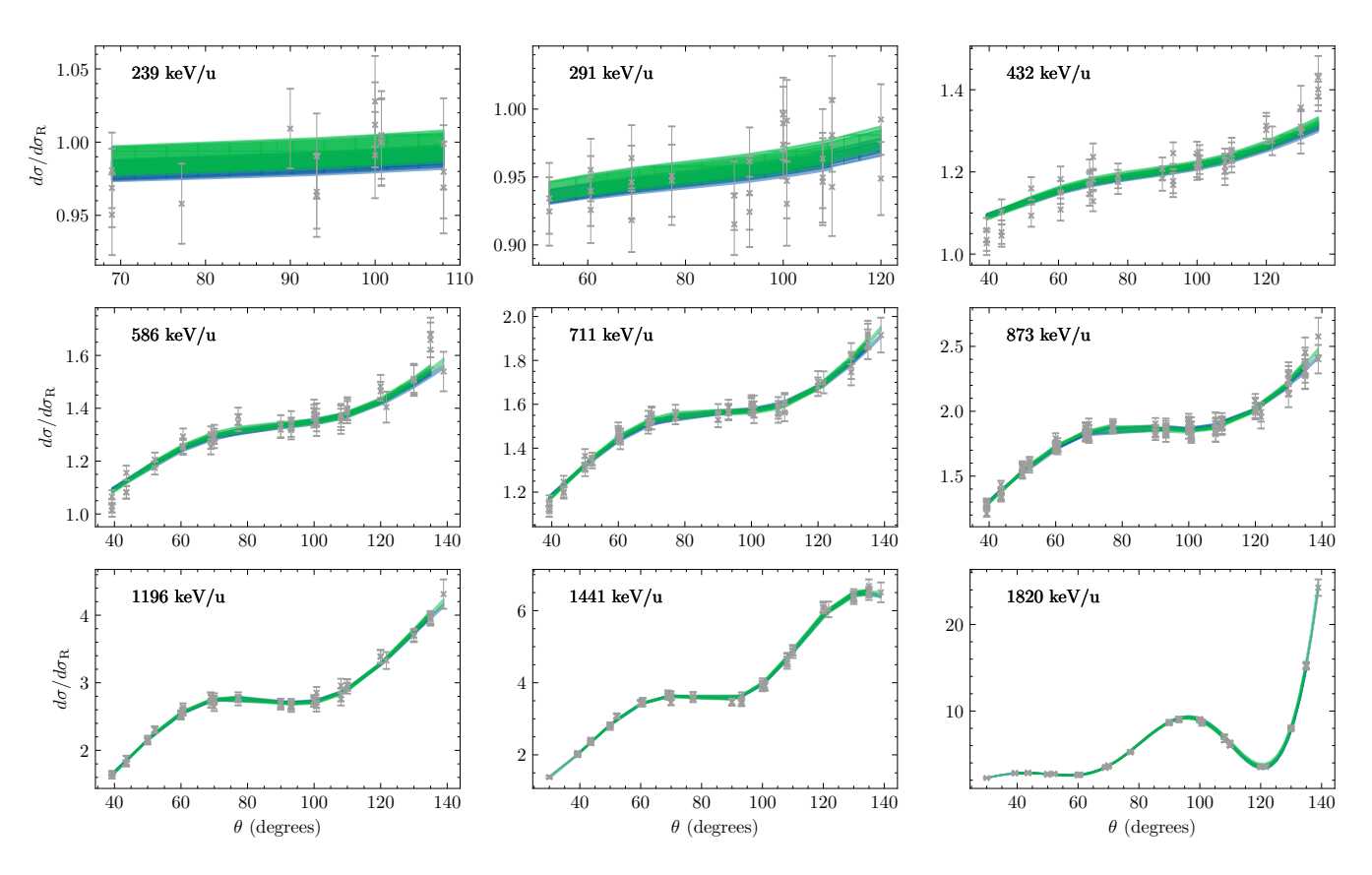


**Figure 5.** Angular dependence of the differential cross sections of Paneru et al. (2022) are shown relative to the Rutherford prediction with grey x's and error bars. Each panel includes the measurements from three interaction regions (Paneru, 2020). Bands indicate 68% intervals. Green bands are generated for the analysis of  $\mathcal{D}_{CS}$ . Blue bands correspond to  $\mathcal{D}_{CSB}$ .

The normalization factors applied to the theory predictions for each of the SONIK energies are shown in Fig.  $\boxed{10}$ . When the data of  $\boxed{\text{Barnard et al.}}$  ( $\boxed{1964}$ ) are included in the analysis, the SONIK normalization factors are significantly larger. This effect is systematically apparent at lower energies. In more than half the cases, the  $\mathcal{D}_{\text{CSB}}$  and  $\mathcal{D}_{\text{CS}}$  results are inconsistent with each other. For eight out of ten SONIK energies, the normalization factor obtained from the fit is within the common-mode error estimated by the SONIK collaboration. Note that the common-mode error in this experiment was estimated to be different at different beam energies ( $\boxed{\text{Paneru}}$ ,  $\boxed{2020}$ )  $\boxed{\text{I}}$ . This is represented in Fig.  $\boxed{\text{10}}$  by the varying heights of the grey bands, which are priors in accord with these experimentally assigned common-mode errors, see Table  $\boxed{\text{2}}$ .

The posteriors for  $f_{\rm Barnard}$  and the energy shifts for both the Barnard et al. (1964) and SONIK (Paneru et al., 2022) data sets (see Sec. 3.3) are shown in Fig. 11. The result for  $f_{\rm Barnard}$  is  $1.002^{+0.003}_{-0.002}$ : well within the estimated systematic uncertainty of 5% given in Barnard et al. (1964). A shift of  $19.26^{+2.90}_{-2.51}$  keV in the energies reported in Barnard et al. (1964) is found, but this result is consistent with the energy uncertainty estimates ranging from 20-40 keV given in that paper. However, even such a clearly nonzero shift does not seem to significantly impact extrapolated quantities. Finally, the SONIK energy shift indicated by our analyses is  $1.59^{+2.43}_{-1.81}$  keV. This result matches very well with the reported energy uncertainty estimate of 3 keV. The prior for this parameter was a normal distribution centered at 0 keV with a 1- $\sigma$  width of 3 keV. The primary difference between the posterior and the prior for this parameter is the loss of probability in

<sup>1</sup> We use slightly different common-mode uncertainty estimates in our prior definitions than those listed in (Paneru, 2020). This update will be reflected in a forthcoming publication by the SONIK collaboration (Paneru et al., 2022)

392

393

394

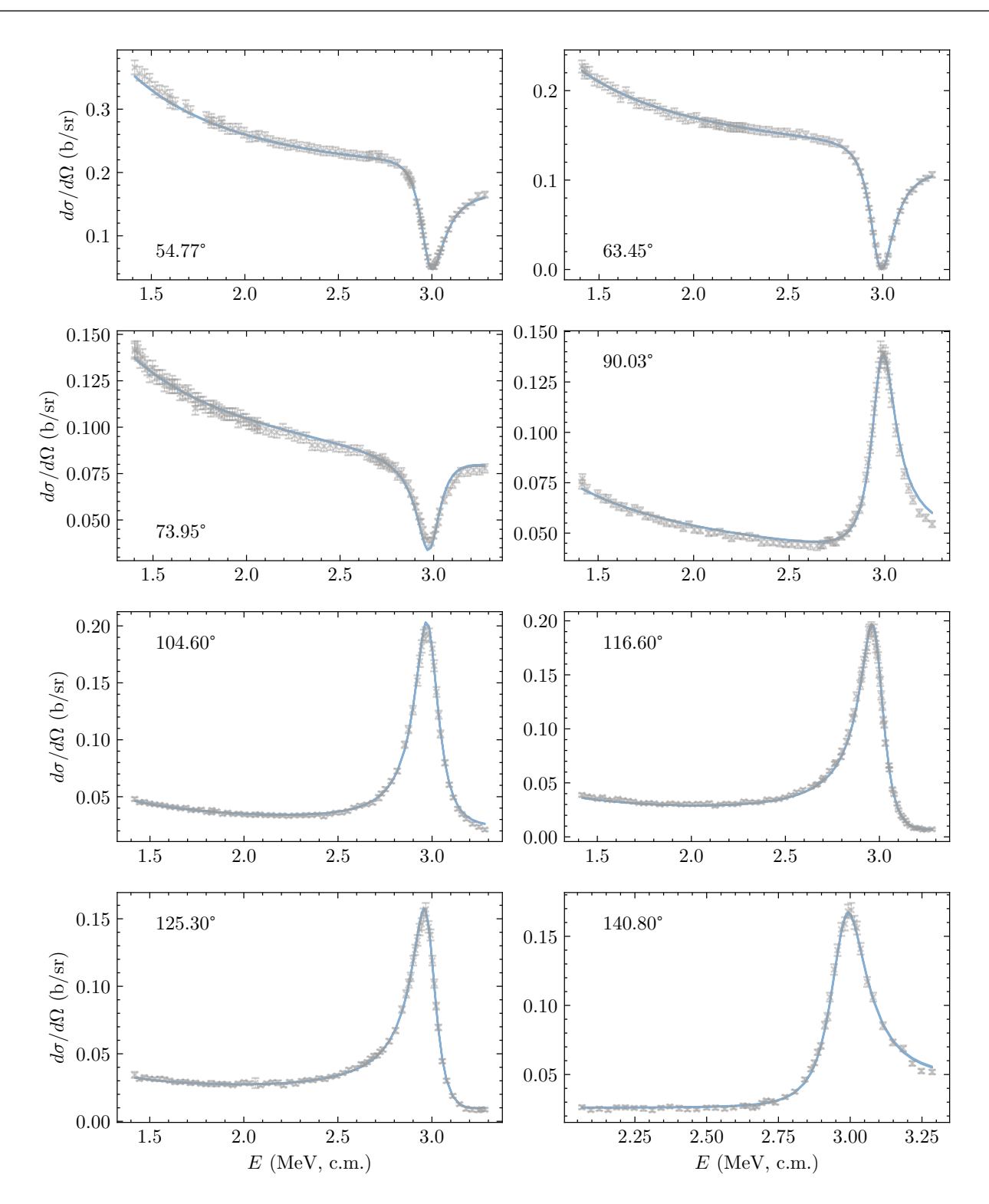


**Figure 6.** Differential cross section as a function of energy as reported in Barnard et al. (1964), shown as grey x's with error bars. Blue bands represent the 68% intervals generated from the  $\mathcal{D}_{CSB}$  analysis.

the negative energy region. If any energy shift in the SONIK data (Paneru et al., 2022) is necessary, it is positive, but since 0 keV is well within one standard deviation, there is strong evidence for no shift.

The ANCs corresponding to the two bound <sup>7</sup>Be states are of particular interest for extrapolating threshold quantities. First, we point out that the inclusion of scattering data significantly reduces the uncertainty

396 397

398

399

400

401

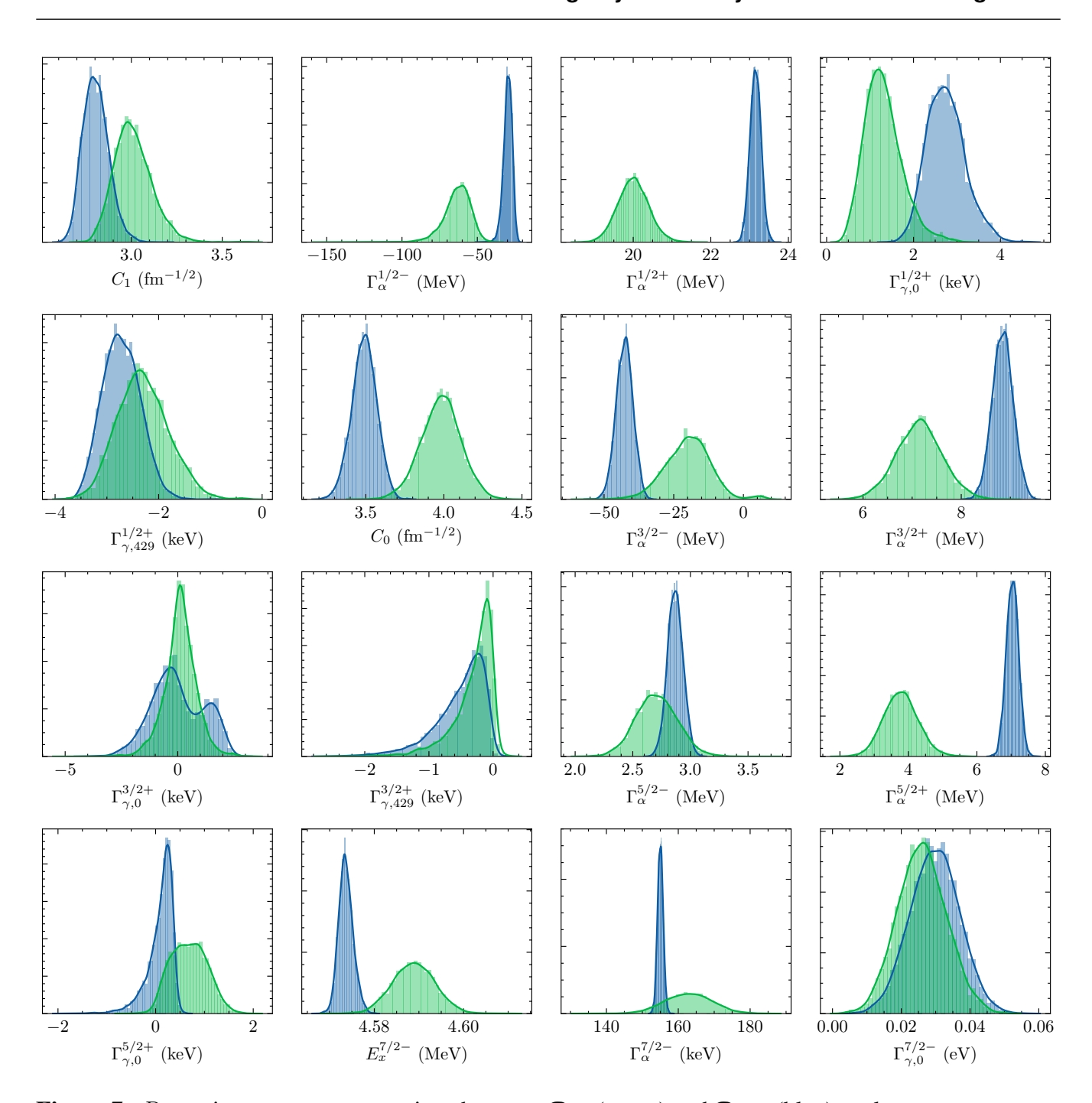


**Figure 7.** R-matrix parameter comparison between  $\mathcal{D}_{CS}$  (green) and  $\mathcal{D}_{CSB}$  (blue) analyses.

of the ANCs. Our posterior is much narrower than that obtained using capture-only data in Zhang et al. (2020). This highlights the importance of scattering data in constraining bound-state properties and the amplitudes associated with transitions to them.

Second, the choice of scattering data set matters. The  $C_1$  results from analyzing  $\mathcal{D}_{\mathrm{CS}}$  and  $\mathcal{D}_{\mathrm{CSB}}$  are discrepant at the 1- $\sigma$  level. The  $C_0$  results disagree by approximately 2- $\sigma$ . The contrast is highlighted in Fig. 12 where the squares  $C_1^2$  and  $C_0^2$  are compared. The differing values directly impact the S-factor extrapolations discussed below.

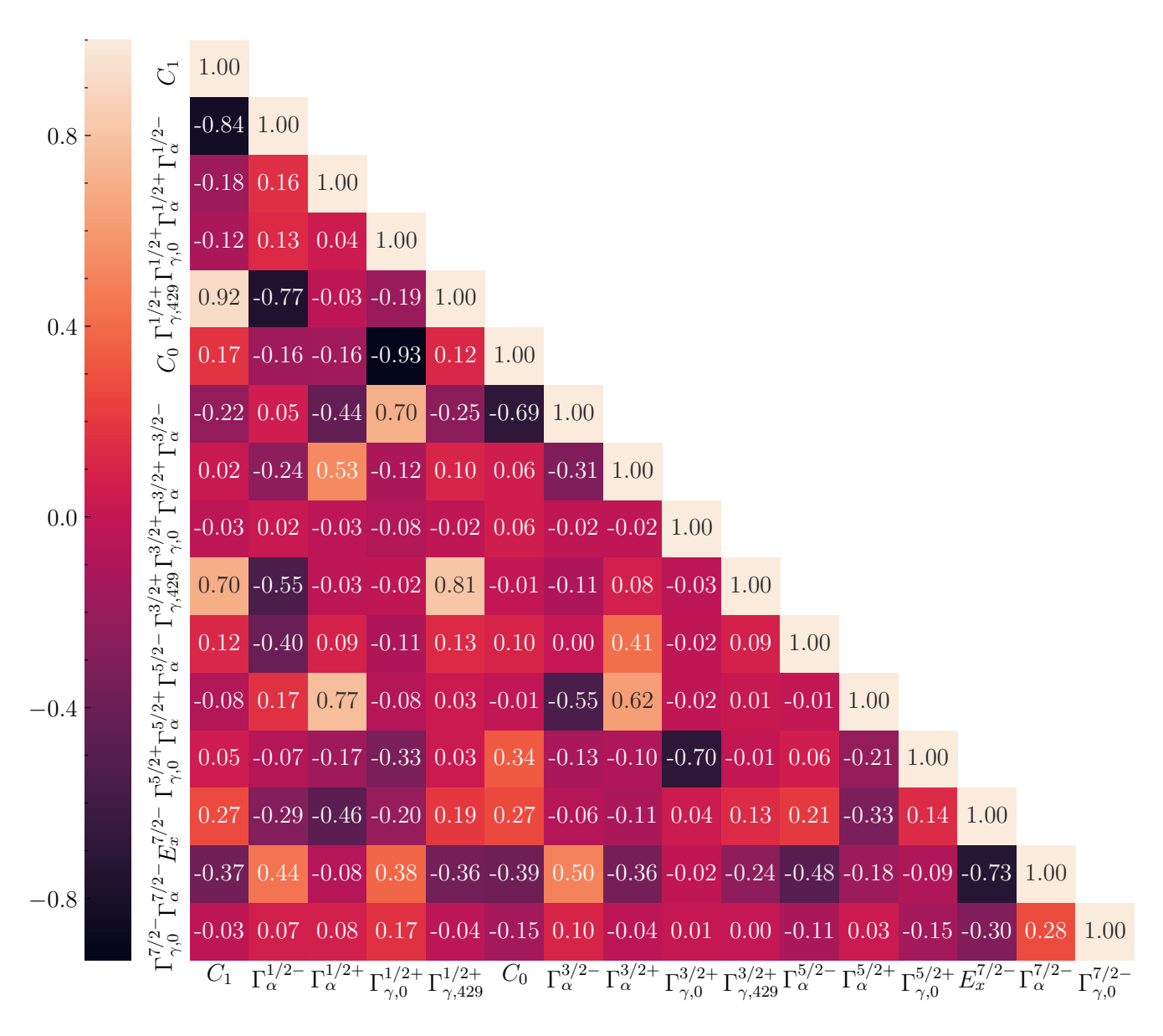


**Figure 8.** Correlation matrix of R-matrix parameters for the  $\mathcal{D}_{CS}$  analysis. Parameter chains are centered at zero and scaled to one prior to the computation. The strongest correlations (anti-correlations) are highlighted with lighter (darker) colors.

#### 402 5.3 Extrapolated quantities

The Coulomb-modified effective range function is given in Hamilton et al. (1973) and van Haeringen (1977) as

$$K(E) = k^{2\ell+1} \frac{\eta^{2\ell}}{\Gamma^2(\ell+1)} u_{\ell}(\eta) \left[ C_0^2(\eta) \cot \delta_{\ell} + 2\eta h(\eta) \right] , \qquad (5)$$

405 where k is the relative momentum,  $\ell$  is the angular momentum,  $\eta$  is the Sommerfeld parameter,  $\Gamma$  is the 406 gamma function,  $u_{\ell}(\eta)$  is given by

$$u_{\ell}(\eta) = \frac{\Gamma^2(2\ell+2)C_{\ell}^2}{(2\eta)^{2\ell}C_0^2} \,, \tag{6}$$

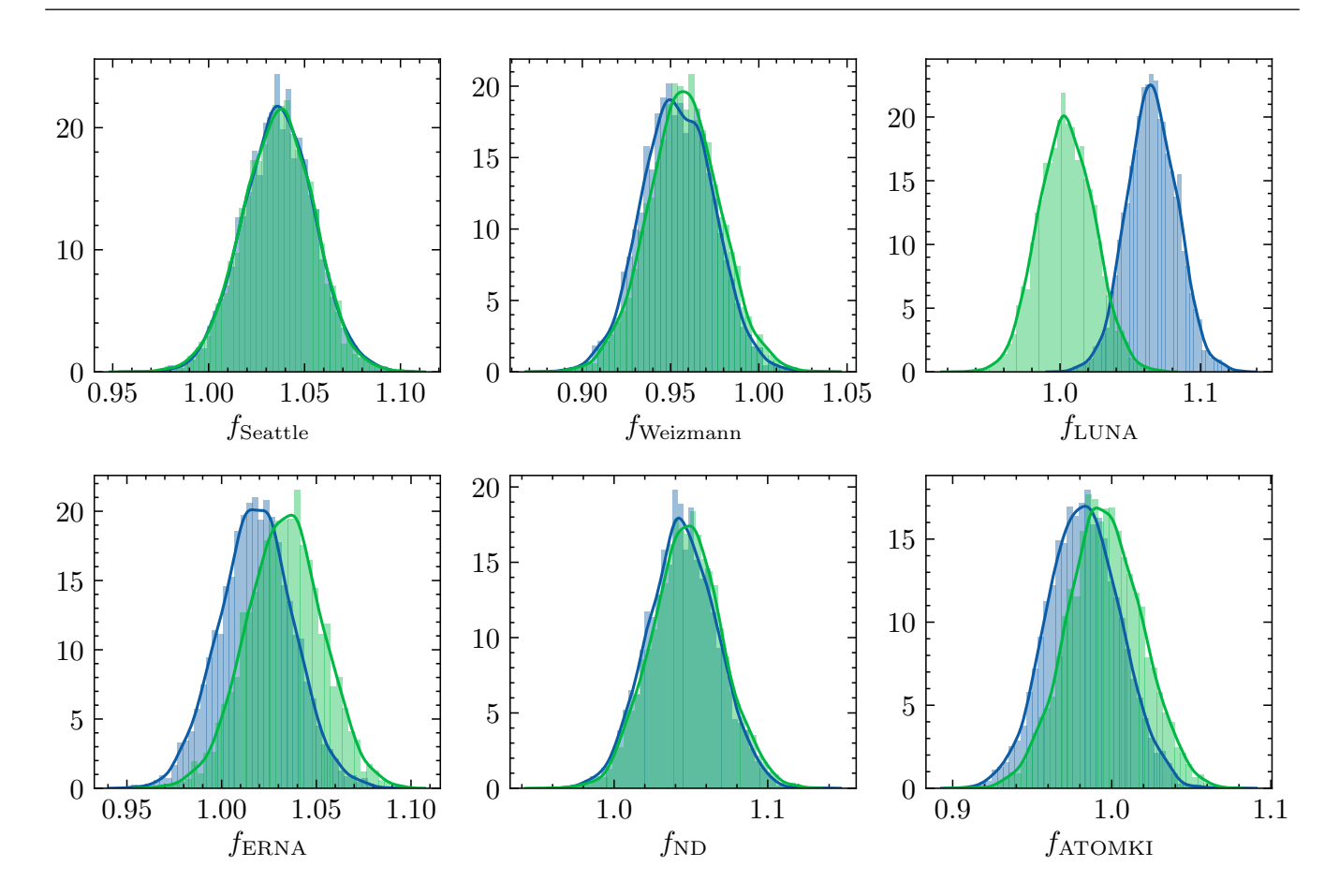


**Figure 9.** The normalization factors applied to the total cross section predicted by our R-matrix model are compared for each of the total capture data sets (Seattle (Brown et al., 2018) Weizmann (Singh et al., 2004), LUNA (Costantini et al., 2008), ERNA (Di Leva et al., 2009), Notre Dame (Kontos et al., 2013), and ATOMKI (Bordeanu et al., 2013)).  $\mathcal{D}_{CSB}$  (blue) and  $\mathcal{D}_{CS}$  (green) results are shown together for each data set.

407 with

$$C_{\ell} = \frac{(\ell^2 + \eta^2)^{1/2}}{\ell(2\ell + 1)} C_{\ell-1} , \qquad (7)$$

$$C_0 = \left[\frac{2\pi\eta}{e^{2\pi\eta} - 1}\right]^{1/2}, (8)$$

$$h(\eta) = \frac{1}{2} \left[ \Psi(1 + i\eta) + \Psi(1 - i\eta) \right] - \ln \eta ,$$
 (9)

and  $\Psi$  representing the digamma function (Humblet, 1985). This effective range function is an analytic function of E (or  $k^2$ ) near E=0. From the phase shifts, obtained with BRICK, calculated over a range of low momenta, one can fit the scattering length,  $a_0$ , and effective range,  $r_0$ , according to the low-energy expansion

$$K(E) = -\frac{1}{a_0} + \frac{r_0}{2}k^2 + \dots$$
 (10)

Our calculation involves 70 equally spaced phase shifts over a range of low energies from 0.57 keV to 3.93 MeV. The results are used to evaluate the effective range function defined by Eq. (5). The energy

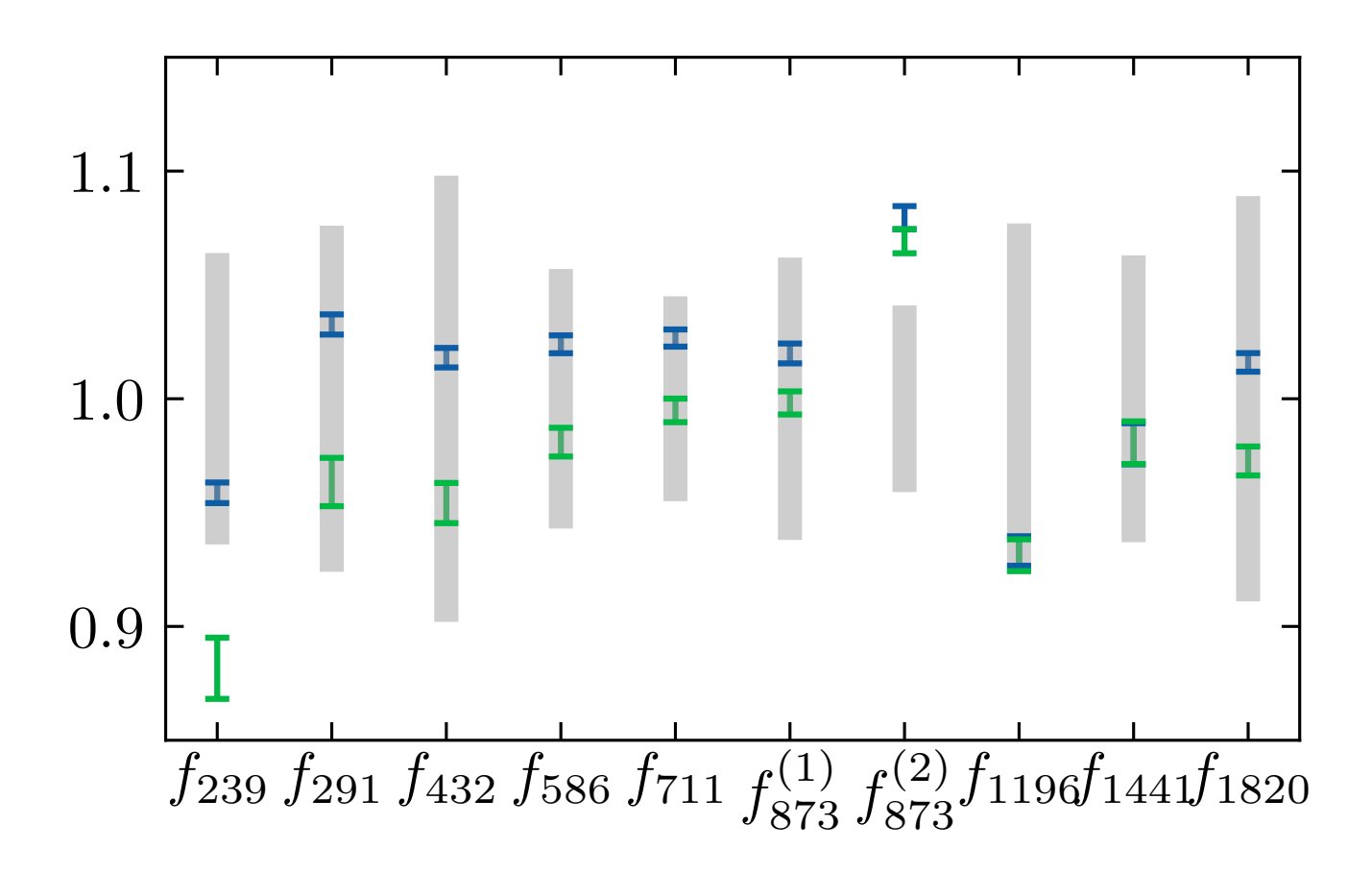


**Figure 10.** Summaries of the normalization factor posteriors for each SONIK (Paneru et al.), 2022) data set are shown for  $\mathcal{D}_{CSB}$  (blue) and  $\mathcal{D}_{CS}$  (green). Error bars represent 68% quantiles. Grey-shaded rectangles indicate the uncertainties reported in (Paneru, 2020).

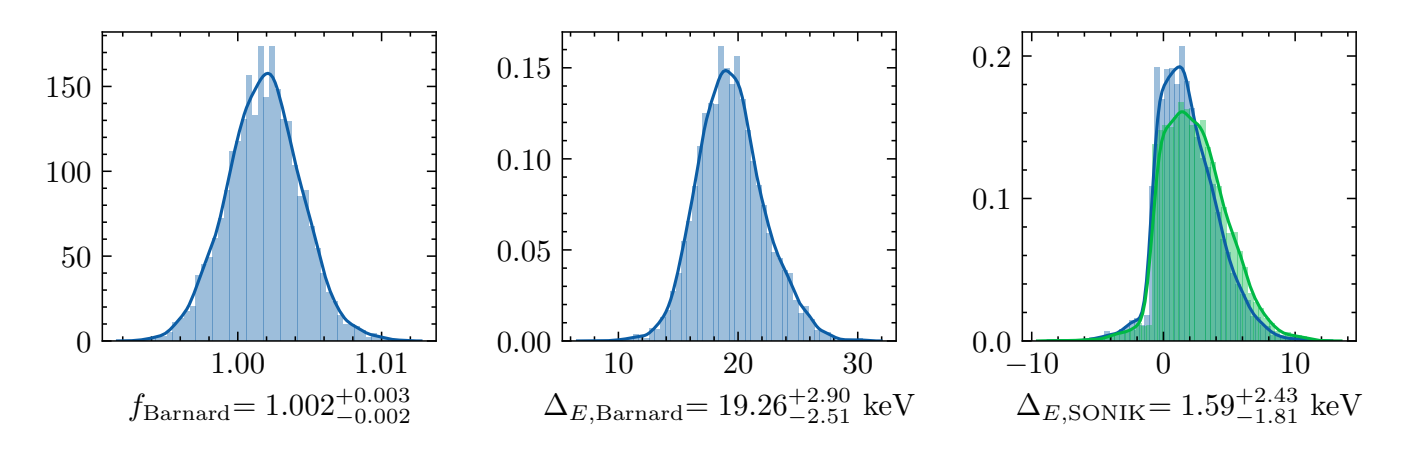


**Figure 11.** Posteriors of the normalization factor applied to the Barnard data and the energy shifts introduced to the Barnard et al. (1964) and SONIK (Paneru et al.), 2022) data sets. The Barnard normalization factor is applied to the theory prediction. Energy shifts are presented in keV. These results were obtained exclusively with the  $\mathcal{D}_{CSB}$  data model.

dependence is then fit to Eq. (10) using a non-linear least squares fit. In addition to  $a_0$  and  $r_0$  defined in Eq. (15), the shape parameter at  $\mathcal{O}(k^4)$  was fit to ensure a better determination of  $a_0$  and  $r_0$ .

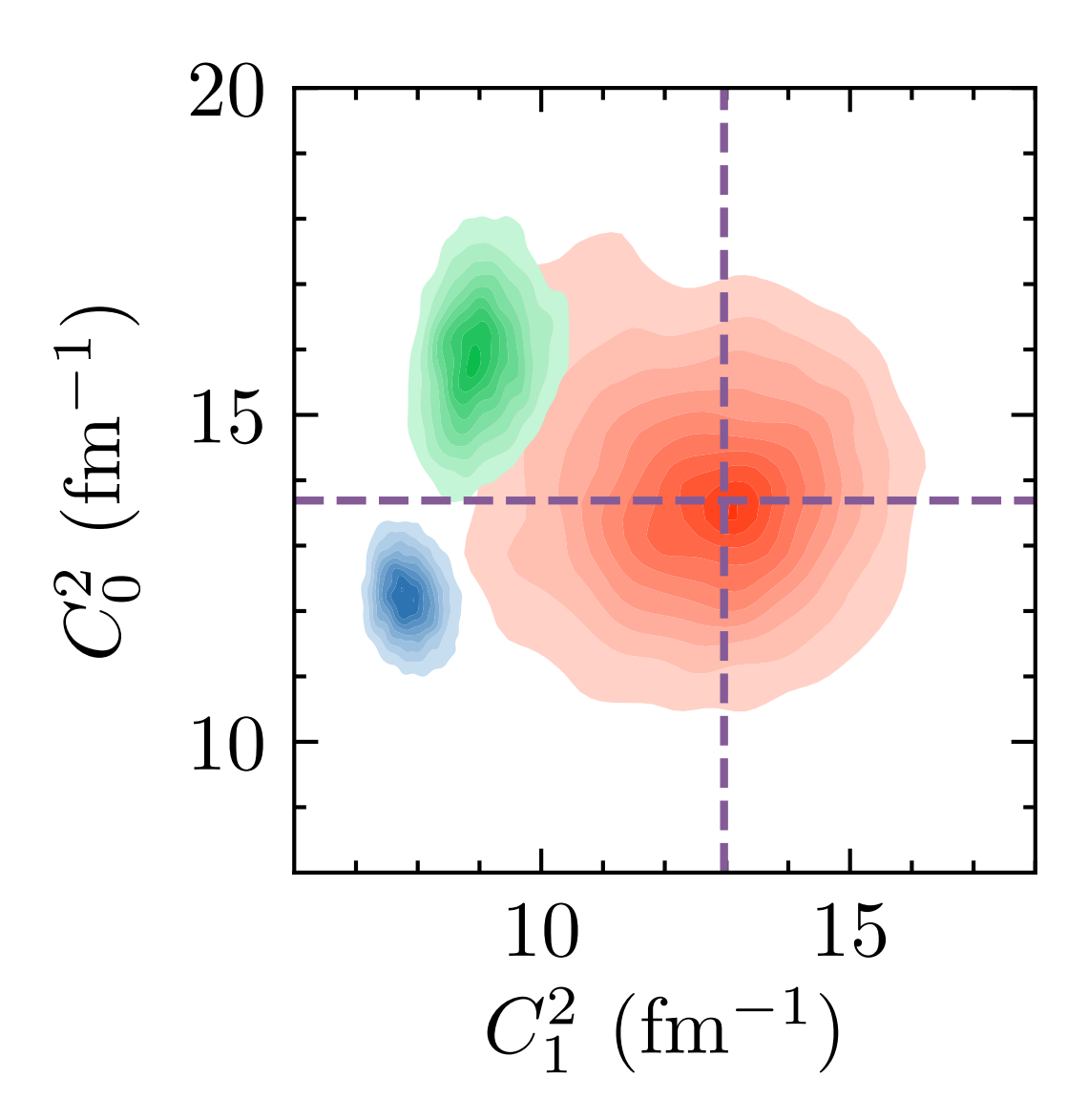


**Figure 12.** The two-dimensional posterior of the squares of the ANCs,  $C_0$  and  $C_1$ . Results for  $\mathcal{D}_{CS}$  are shown in green and for  $\mathcal{D}_{CSB}$  in blue. The EFT analysis of capture data of Zhang et al. (2020) extracted the ANC values shown in red, and in the analysis of Barnard et al. (1964) and capture data of deBoer et al. (2014) the ANCs were fixed at the location indicated by the purple, dashed lines.

- The results from  $\mathcal{D}_{CSB}$  and  $\mathcal{D}_{CS}$  are shown in Fig. [13] As in the ANC comparison, they are strikingly discrepant. The naive expectation would be that  $\mathcal{D}_{CSB}$  distributions would be smaller subsets of the  $\mathcal{D}_{CS}$  distributions. For many relevant quantities, this is not the case.
- Figure 14 shows a comparison of the scattering lengths obtained from the  $\mathcal{D}_{CS}$  and  $\mathcal{D}_{CSB}$  analyses. A comparison to Zhang et al. (2020), also included in Figure 14, reveals the impact of including scattering data: the inclusion of scattering data drives the median downward and constrains the uncertainties significantly.
- 422 A summary of these posteriors is given in Table 4.
- The  $\mathcal{D}_{\mathrm{CSB}}$  scattering length and effective range are both smaller and more tightly constrained. One might have expected that with more data—and more data at lower energies—this extrapolated quantity would become more tightly constrained. The two-dimensional posteriors shown in Fig. 13 seem to lie on the same

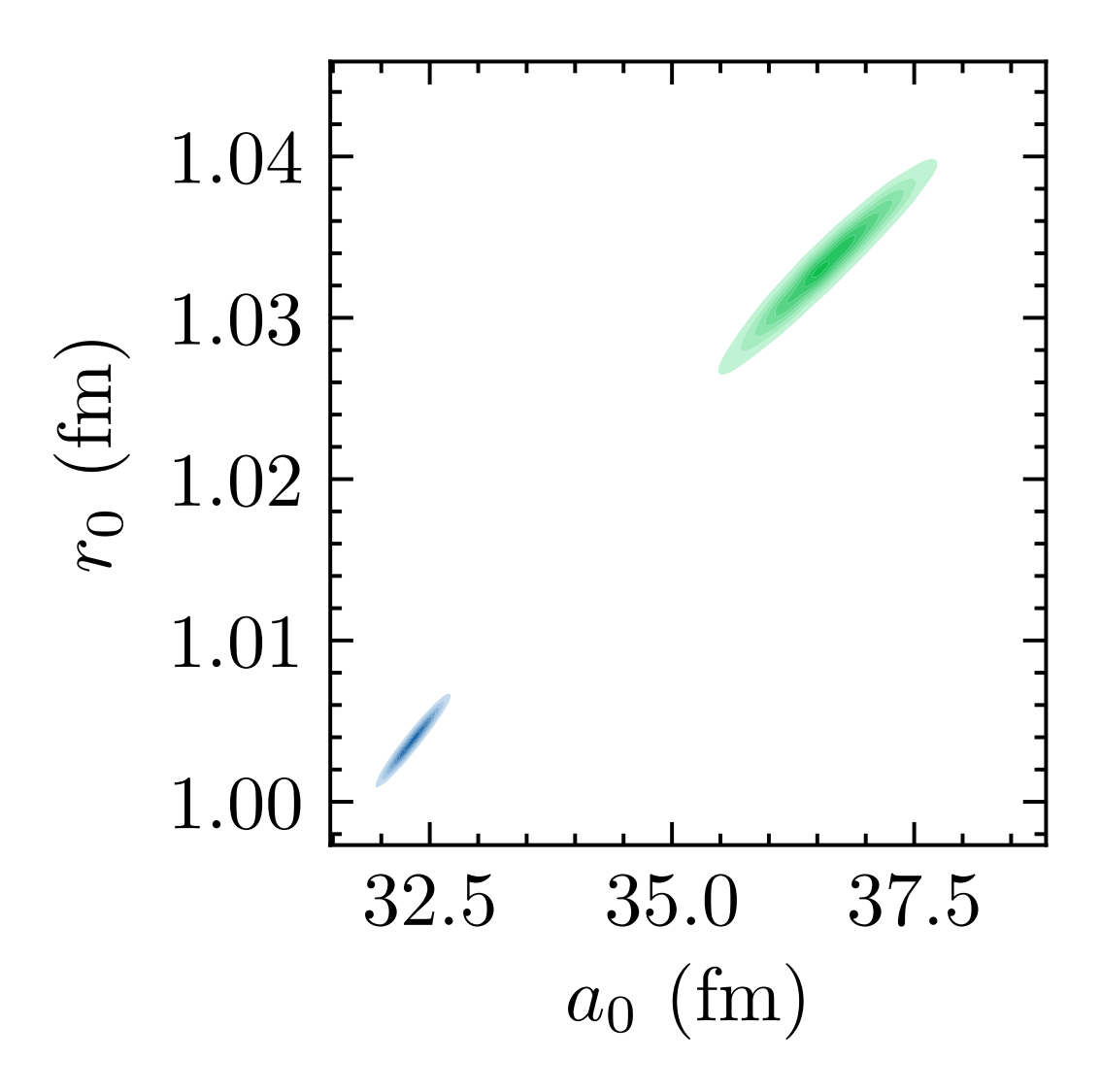


**Figure 13.**  $a_0$ - $r_0$  correlation for both  $\mathcal{D}_{CSB}$  (blue) and  $\mathcal{D}_{CS}$  (green) data models.

line or band that defines the correlation between  $a_0$  and  $r_0$ , though two extended posteriors is not sufficient to define such a line.

The total capture S factor at zero energy was extrapolated by evaluating the S factor at 100 evenly spaced points between 1 to 100 keV, constructing a cubic-polynomial interpolation function to represent the calculations, and evaluating that function at zero energy. Errors from the interpolation/extrapolation process are negligible when compared to contributions from parameter uncertainties. The results are shown alongside previous results in Fig. 15 As expected from the different low-energy behaviors shown in Fig. 15 the  $\mathcal{D}_{CS}$  and  $\mathcal{D}_{CSB}$  results are discrepant, only overlapping at the 2- $\sigma$  level. The inclusion of the Barnard et al. (1964) data reduces the uncertainty in S(0) and pulls the entire distribution downward, outside the uncertainties of the  $\mathcal{D}_{CS}$  analysis. This effect is not seen in (deBoer et al., 2014) because the ANCs in that analysis were not varied freely. The  $\mathcal{D}_{CSB}$  result is discrepant with the  $\mathcal{D}_{CS}$  results and those reported in (deBoer et al., 2014) and (Zhang et al., 2020). A summary of these posteriors is given in Table 4.

Insights into the relevance of parameters can be obtained by examining the correlations between them. In Fig. 16, the correlations between S(0) and  $a_0$ ,  $C_1^2$  and  $C_0^2$  are shown. While the  $\mathcal{D}_{CS}$  and  $\mathcal{D}_{CSB}$  results are discrepant in several astrophysically relevant cases, the discrepancy is consistent, and this figure exposes,

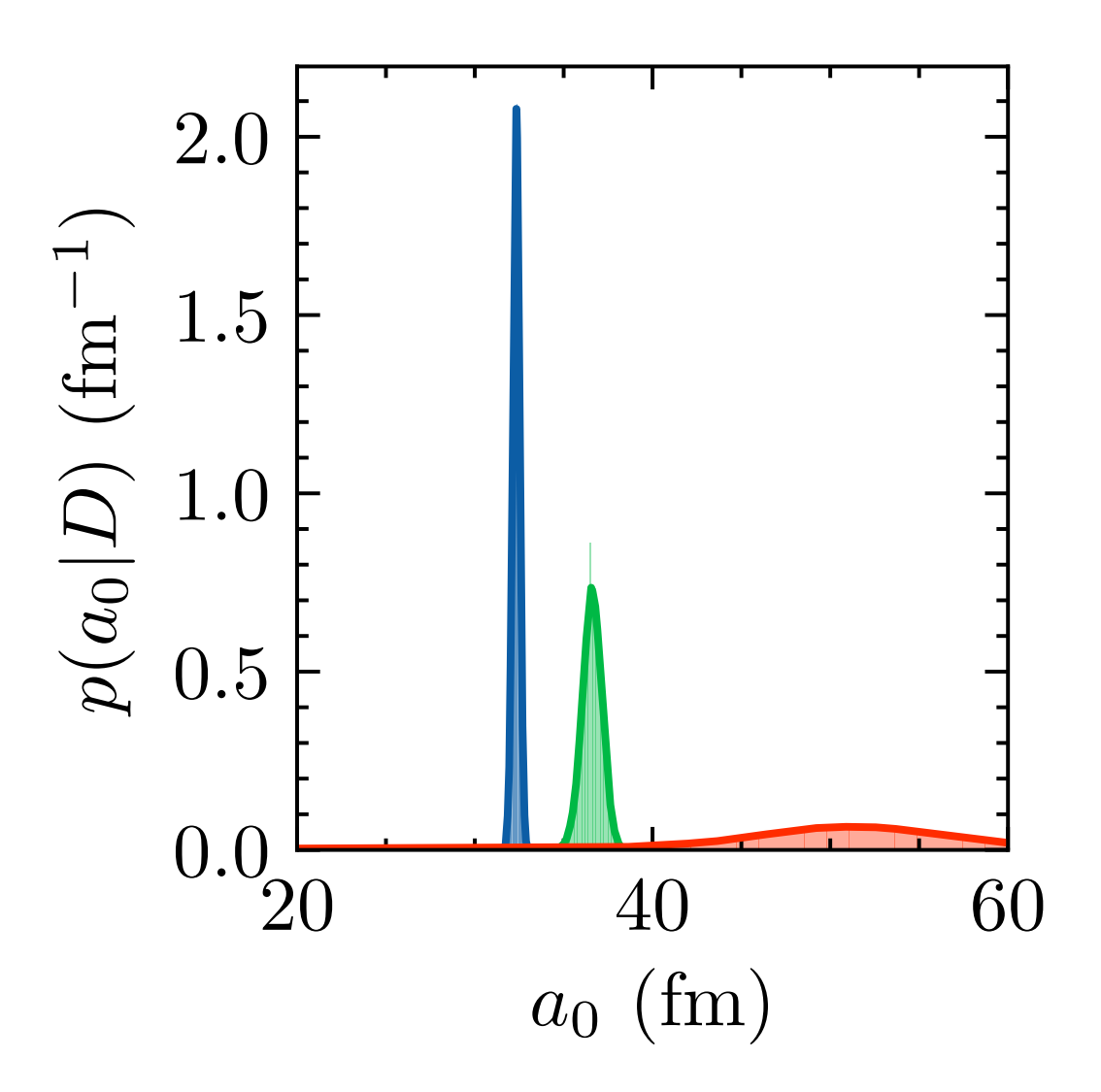


**Figure 14.**  $a_0$  posteriors obtained from  $\mathcal{D}_{CS}$  (green) and  $\mathcal{D}_{CSB}$  (blue) analyses. The result from Zhang et al. (2020) is shown in red.

Analysis	S(0) (keV b)	$a_0$ (fm)	$r_0$ (fm)
$\mathcal{D}_{ ext{CS}}$	$0.539^{+0.011}_{-0.012}$	$36.59^{+0.55}_{-0.53}$	$1.033^{+0.003}_{-0.003}$
$\mathcal{D}_{ ext{CSB}}$	$0.495^{+0.008}_{-0.008}$	$32.32_{-0.18}^{+0.18}$	$1.004^{+0.001}_{-0.001}$
deBoer et al. (2014)	$\begin{array}{ c c c c c c c c c c c c c c c c c c c$	_	
Zhang et al. (2020)	$0.578^{+0.015}_{-0.016}$	$50.36^{+6.02}_{-7.50}$	$0.974^{+0.025}_{-0.027}$

**Table 4.** A summary of the posteriors of the extrapolated quantities. Where possible, results from other anlayses are included.

- 441 to a large extent, why: the ANCs, particularly the ground-state ANC, strongly correlates with S(0). The
- Barnard et al. (1964) data more tightly constrain these parameters at smaller values, and this directly lowers
- 443 the predicted S(0) extrapolation.

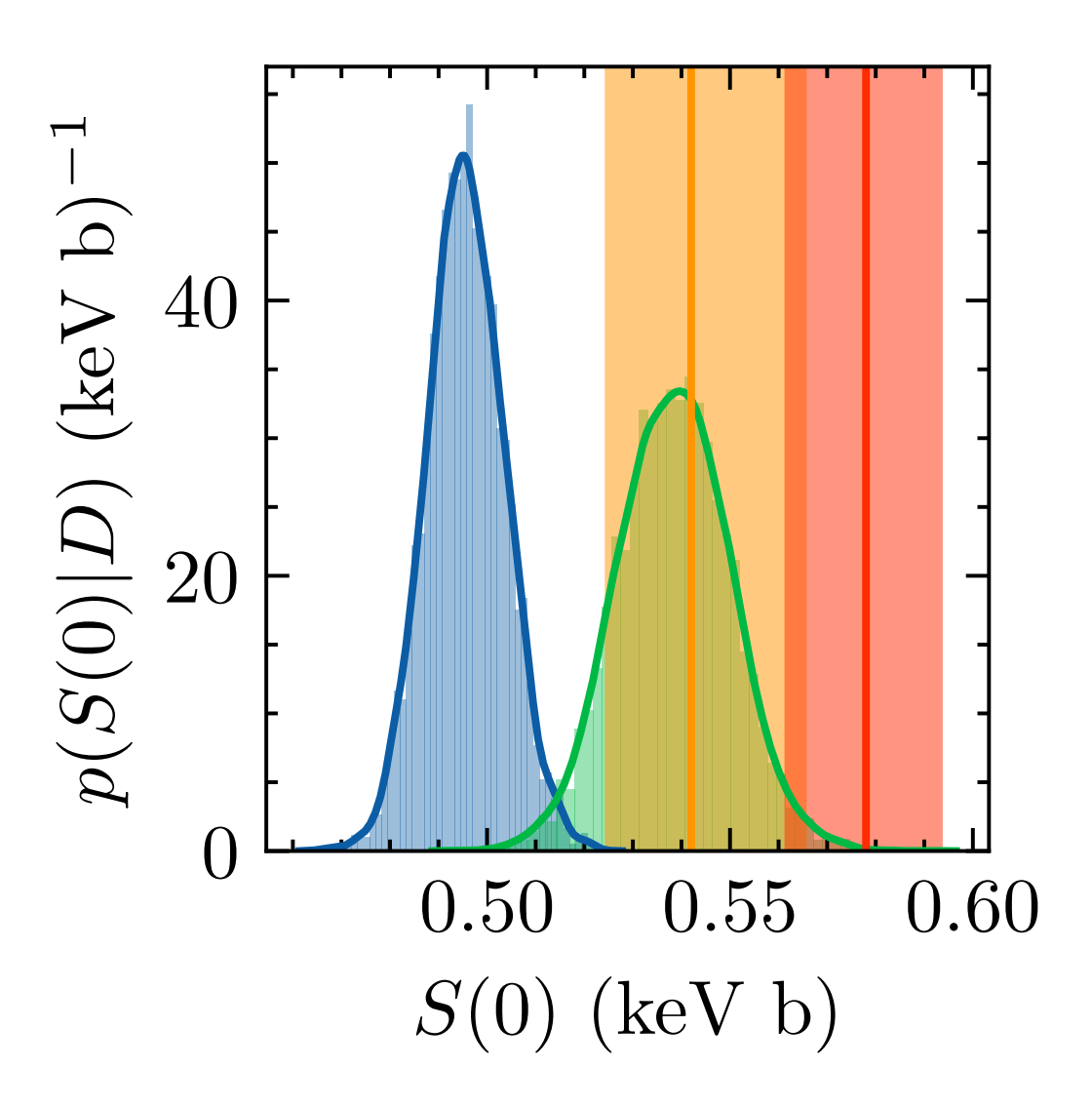


**Figure 15.** Extrapolated S(0) posteriors from the analyses of both  $\mathcal{D}_{CSB}$  (blue) and  $\mathcal{D}_{CS}$  (green) data models. Previous results from Zhang et al. (2020) (red) are deBoer et al. (2014) (orange) are also summarized here for comparison.

## 6 CONCLUSIONS

450

451

452

453

454

455

We have described and applied the Bayesian R-matrix Inference Code Kit (BRICK), which facilitates communication between the phenomenological R-matrix code AZURE2 (Azuma et al., 2010) and a Markov Chain Monte Carlo (MCMC) sampler such as emcee (Foreman-Mackey et al., 2013). It thereby enables MCMC sampling of the joint posterior probability density function (pdf) for the R-matrix parameters and normalization factors. With samples that represent such a posterior in hand, the computation of the pdf for any quantity that can be calculated in the R-matrix formalism is straightforward.

While BRICK is a general tool, we have also provided an example of its application to an R-matrix fit of  ${}^{3}\text{He-}\alpha$  scattering and the  ${}^{3}\text{He}(\alpha,\gamma){}^{7}\text{Be}$  capture reaction data, in order to make inferences about the  ${}^{7}\text{Be}$  system. This application was partly motivated by the availability of a new  ${}^{3}\text{He-}\alpha$  scattering data set obtained using the SONIK detector at TRIUMF (Paneru, 2020) following the suggestion of deBoer et al. (2014). These data have more carefully quantified uncertainties than a previous measurement by Barnard et al. (1964). Our study shows this motivation was well justified, finding discrepant values

- for extrapolated quantifies when the data of Barnard et al. (1964) were included. Our analysis of the SONIK data shows consistency between them and capture data, producing an S factor in accord with analyses of capture data alone: our final  $\mathcal{D}_{CS}$  (capture + SONIK data) result for the S-factor at zero energy is  $S(0) = 0.539^{+0.011}_{-0.012}$  keV b. When the Barnard et al. (1964) data were included in the analysis, the  $\mathcal{D}_{CSB}$  results produced significantly lower ANCs and S(0) extrapolation. Indeed, the  $\mathcal{D}_{CSB}$  analysis produces values for S(E) at c.m. energies of 10–20 keV that can only be reconciled with the LUNA data (Costantini et al., 2008) if the normalization of these data is adjusted by 2–3 times the quoted common-mode error.
- This emphasizes the importance of detailed uncertainty quantification when data sets are to be used for accurate inference of extrapolated quantities, where Barnard et al. (1964) does not include these kinds of details regarding the experiment. This makes the tension between the Barnard et al. (1964) and SONIK data regarding S(0) difficult to resolve, thus the Barnard et al. (1964) data may need to be omitted from future evaluations. We emphasize, though, that these previous data were invaluable in advancing our understanding of the  $^7$ Be system to its current state, but data with more well defined uncertainties are needed for current applications.
- Zhang, Nollett, and Phillips pointed out that the s-wave  ${}^{3}\text{He-}\alpha$  scattering length is correlated with this result (Zhang et al., 2020). The  $\mathcal{D}_{CS}$  analysis produces  $a_0 = 36.59^{+0.55}_{-0.53}$  fm. Premarathna and Rupak simultaneously analysed capture data and  ${}^{3}\text{He-}\alpha$  phase shifts in EFT and found  $a_0 = 40^{+5}_{-6}$  fm (Model A II of Premarathna and Rupak (2020a))—in good agreement with this number. However, it disagrees by  $2\sigma$  with the  $a_0$  extracted using EFT methods from capture data alone by Zhang et al. (2020):  $a_0 = 50^{+6}_{-7}$ . Recently Poudel and Phillips (2021) performed an EFT analysis of the SONIK data, using priors on the  ${}^{7}\text{Be}$  ANCs from the capture analysis of Zhang et al. (2020), and extracted  $a_0 = 60 \pm 6$  fm—even further away from the results of this R-matrix analysis.
- Improvements in the analyses presented here could occur if there were:
- Better documentation of the energy dependence of systematic uncertainties in published data sets.
   The Bayesian formalism that underlies BRICK allows systematic uncertainties with any correlation structure to be incorporated into the analysis.
- Improved understanding of the way theory uncertainties in the phenomenological *R*-matrix formalism affect the extrapolation of data.
- Detailed modern data with full uncertainty quantification in the vicinity of the  $7/2^-$  resonance. This may help resolve some of the ambiguities in results between the  $\mathcal{D}_{CS}$  and  $\mathcal{D}_{CSB}$  analyses.
- Ab initio constraints, e.g., on ANCs could be incorporated in the analysis.
- Data from transfer reactions that provided complementary information on the <sup>7</sup>Be ANCs.
- Future applications of BRICK could include posteriors for astrophysical reaction rates. This would enhance BRICK's utility as a tool for performing detailed uncertainty quantification on nuclear reactions, especially those of astrophysical interest. AZURE2 already includes the necessary functionality.
- 492 Implementing this feature ought to be a straightforward process.

#### **CONFLICT OF INTEREST STATEMENT**

The authors declare that the research was conducted in the absence of any commercial or financial relationships that could be construed as a potential conflict of interest.

#### **AUTHOR CONTRIBUTIONS**

- 495 CB and DP formulated the conceptual design of the project. DO was the author of the BRICK code and was
- 496 the author of the first draft of the manuscript. RD consulted DO to facilitate the interface of the BRICK with
- 497 AZURE2 codes, perform benchmark calculations, and the calculations for the <sup>7</sup>Be system. SP supplied their
- 498 experimental data for the calculations and consulted on its analysis. CB and RD collected and interpreted
- 499 past experimental data from the literature. All authors contributed to the critical discussions of the research,
- 500 writing, revising, reading, and approving the submitted manuscript.

### **FUNDING**

- 501 This work was supported by the U.S. Department of Energy, National Nuclear Security Agency under
- 502 Award DE-NA0003883, and Office of Science, Office of Nuclear Physics, under Award DE-FG02-93ER-
- 503 40756, as well as by the National Science Foundation under grants OAC-2004601 (CSSI program, BAND
- 504 collaboration), PHY-2011890 (University of Notre Dame Nuclear Science Laboratory), and PHY-1430152
- 505 (the Joint Institute for Nuclear Astrophysics Center for the Evolution of the Elements). This research
- 506 utilized resources from the Notre Dame Center for Research Computing.

#### **ACKNOWLEDGMENTS**

507 We thank Maheshwor Poudel and Xilin Zhang for helpful discussions.

#### SUPPLEMENTAL DATA

- 508 Supplementary Material should be uploaded separately on submission, if there are Supplementary Figures,
- 509 please include the caption in the same file as the figure. LaTeX Supplementary Material templates can be
- 510 found in the Frontiers LaTeX folder.

#### **REFERENCES**

- 511 Lane AM, Thomas RG. R-Matrix Theory of Nuclear Reactions. Rev. Mod. Phys. 30 (1958) 257–353.
- 512 doi:10.1103/RevModPhys.30.257.
- 513 Brown D, Chadwick M, Capote R, Kahler A, Trkov A, Herman M, et al. ENDF/B-VIII.0: The 8th Major
- Release of the Nuclear Reaction Data Library with CIELO-project Cross Sections, New Standards and
- Thermal Scattering Data. *Nuclear Data Sheets* **148** (2018) 1–142. doi:https://doi.org/10.1016/j.nds.2018.
- 516 02.001. Special Issue on Nuclear Reaction Data.
- 517 Azuma RE, Uberseder E, Simpson EC, Brune CR, Costantini H, de Boer RJ, et al. AZURE: An R-matrix
- code for nuclear astrophysics. *Phys. Rev. C* **81** (2010) 045805. doi:10.1103/PhysRevC.81.045805.
- 519 Descouvement P, Adahchour A, Angulo C, Coc A, Vangioni-Flam E. Big-Bang reaction rates within the
- 520 R-matrix model. Nuclear Physics A **758** (2005) 783–786. doi:https://doi.org/10.1016/j.nuclphysa.2005.
- 521 05.140. Nuclei in the Cosmos VIII.
- 522 ENSDF (2022). From ENSDF database as of April 12, 2022. Version available at
- 523 http://www.nndc.bnl.gov/ensarchivals/.
- 524 Smith DL, Badikov SA, Gai EV, Oh SY, T Kawano NML, Pronyaev VG. Perspectives on Peelle's Pertinent
- Puzzle. International Evaluation of Neutron Cross-Section Standards (Wagramer Strasse 5, P.O. Box
- 526 100, 1400 Vienna, Austria: International Atomic Energy Agency) (2007), 46–83.

- deBoer RJ, Görres J, Smith K, Uberseder E, Wiescher M, Kontos A, et al. Monte Carlo uncertainty of the  $^3$ He( $\alpha$ ,  $\gamma$ ) $^7$ Be reaction rate. *Phys. Rev. C* **90** (2014) 035804. doi:10.1103/PhysRevC.90.035804.
- 529 Schindler MR, Phillips DR. Bayesian Methods for Parameter Estimation in Effective Field Theories.
- 530 Annals Phys. **324** (2009) 682–708. doi:10.1016/j.aop.2008.09.003,10.1016/j.aop.2009.05.007.
- 531 Furnstahl RJ, Phillips DR, Wesolowski S. A recipe for EFT uncertainty quantification in nuclear physics.
- 532 *J. Phys. G* **42** (2015a) 034028. doi:10.1088/0954-3899/42/3/034028.
- 533 Furnstahl RJ, Klco N, Phillips DR, Wesolowski S. Quantifying truncation errors in effective field theory.
- 534 *Phys. Rev. C* **92** (2015b) 024005. doi:10.1103/PhysRevC.92.024005.
- 535 Zhang X, Nollett KM, Phillips DR. Halo effective field theory constrains the solar  $^7\text{Be} + \text{p} \rightarrow ^8\text{B} + \gamma$  rate.
- 536 *Phys. Lett. B* **751** (2015) 535–540. doi:10.1016/j.physletb.2015.11.005.
- 537 Melendez JA, Wesolowski S, Furnstahl RJ. Bayesian truncation errors in chiral effective field theory:
- nucleon-nucleon observables. *Phys. Rev. C* **96** (2017) 024003. doi:10.1103/PhysRevC.96.024003.
- 539 Wesolowski S, Furnstahl RJ, Melendez JA, Phillips DR. Exploring Bayesian parameter estimation
- for chiral effective field theory using nucleon–nucleon phase shifts. J. Phys. G 46 (2019) 045102.
- 541 doi:10.1088/1361-6471/aaf5fc.
- 542 Neufcourt L, Cao Y, Giuliani S, Nazarewicz W, Olsen E, Tarasov OB. Beyond the proton drip line:
- Bayesian analysis of proton-emitting nuclei. *Phys. Rev. C* **101** (2020a) 014319. doi:10.1103/PhysRevC.
- 544 101.014319.
- Neufcourt L, Cao Y, Nazarewicz W, Olsen E, Viens F. Neutron drip line in the Ca region from Bayesian
- model averaging. *Phys. Rev. Lett.* **122** (2019) 062502. doi:10.1103/PhysRevLett.122.062502.
- 547 King GB, Lovell AE, Neufcourt L, Nunes FM. Direct comparison between Bayesian and frequentist
- uncertainty quantification for nuclear reactions. *Phys. Rev. Lett.* **122** (2019) 232502. doi:10.1103/
- 549 PhysRevLett.122.232502.
- 550 Melendez JA, Furnstahl RJ, Phillips DR, Pratola MT, Wesolowski S. Quantifying Correlated Truncation
- Errors in Effective Field Theory. *Phys. Rev. C* **100** (2019) 044001. doi:10.1103/PhysRevC.100.044001.
- 552 Filin AA, Baru V, Epelbaum E, Krebs H, Möller D, Reinert P. Extraction of the neutron charge radius
- from a precision calculation of the deuteron structure radius. *Phys. Rev. Lett.* **124** (2020) 082501.
- doi:10.1103/PhysRevLett.124.082501.
- 555 Drischler C, Furnstahl RJ, Melendez JA, Phillips DR. How Well Do We Know the Neutron-Matter Equation
- of State at the Densities Inside Neutron Stars? A Bayesian Approach with Correlated Uncertainties.
- 557 Phys. Rev. Lett. 125 (2020a) 202702. doi:10.1103/PhysRevLett.125.202702.
- 558 Drischler C, Melendez JA, Furnstahl RJ, Phillips DR. Quantifying uncertainties and correlations in the
- nuclear-matter equation of state. *Phys. Rev. C* **102** (2020b) 054315. doi:10.1103/PhysRevC.102.054315.
- Premarathna P, Rupak G. Bayesian analysis of capture reactions  ${}^{3}\text{He}(\alpha,\gamma){}^{7}\text{Be}$  and  ${}^{3}\text{H}(\alpha,\gamma){}^{7}\text{Li}$ . Eur. Phys.
- 561 *J. A* **56** (2020a) 166. doi:10.1140/epja/s10050-020-00113-z.
- 562 Zhang X, Nollett KM, Phillips DR. S-factor and scattering-parameter extractions from  ${}^{3}\text{He} + {}^{4}\text{He} \rightarrow$
- <sup>7</sup>Be +  $\gamma$ . J. Phys. G **47** (2020) 054002. doi:10.1088/1361-6471/ab6a71.
- 564 Filin AA, Möller D, Baru V, Epelbaum E, Krebs H, Reinert P. High-accuracy calculation of the deuteron
- charge and quadrupole form factors in chiral effective field theory. *Phys. Rev. C* **103** (2021) 024313.
- doi:10.1103/PhysRevC.103.024313.
- 567 Schunck N, Quinlan KR, Bernstein J. A Bayesian Analysis of Nuclear Deformation Properties with Skyrme
- 568 Energy Functionals. J. Phys. G 47 (2020) 104002. doi:10.1088/1361-6471/aba4fa.
- 569 Neufcourt L, Cao Y, Giuliani SA, Nazarewicz W, Olsen E, Tarasov OB. Quantified limits of the nuclear
- landscape. *Phys. Rev. C* **101** (2020b) 044307. doi:10.1103/PhysRevC.101.044307.

- Everett D, et al. Multisystem Bayesian constraints on the transport coefficients of QCD matter. Phys. Rev. C 103 (2021) 054904. doi:10.1103/PhysRevC.103.054904. 572
- Catacora-Rios M, King GB, Lovell AE, Nunes FM. Statistical tools for a better optical model. Phys. Rev. 573 C 104 (2021) 064611. doi:10.1103/PhysRevC.104.064611. 574
- Reinert P, Krebs H, Epelbaum E. Precision determination of pion-nucleon coupling constants using 575 576 effective field theory. Phys. Rev. Lett. 126 (2021) 092501. doi:10.1103/PhysRevLett.126.092501.
- 577 Phillips DR, Furnstahl RJ, Heinz U, Maiti T, Nazarewicz W, Nunes FM, et al. Get on the BAND Wagon: A
- Bayesian Framework for Quantifying Model Uncertainties in Nuclear Dynamics. J. Phys. G 48 (2021) 578
- 579 072001. doi:10.1088/1361-6471/abf1df.
- Wesolowski S, Svensson I, Ekström A, Forssén C, Furnstahl RJ, Melendez JA, et al. Rigorous constraints 580
- on three-nucleon forces in chiral effective field theory from fast and accurate calculations of few-body 581
- observables. Phys. Rev. C 104 (2021) 064001. doi:10.1103/PhysRevC.104.064001. 582
- Schnabel G, Capote R, Koning A, Brown D. Nuclear data evaluation with Bayesian networks (2021). 583
- Xu J, Zhang Z, Li BA. Bayesian uncertainty quantification for nuclear matter incompressibility. Phys. Rev. 584 C 104 (2021) 054324. doi:10.1103/PhysRevC.104.054324. 585
- Cao S, et al. Determining the jet transport coefficient  $\hat{q}$  from inclusive hadron suppression measurements 586
- using Bayesian parameter estimation. Phys. Rev. C 104 (2021) 024905. doi:10.1103/PhysRevC.104. 587 024905. 588
- Hamaker A, et al. Precision mass measurement of lightweight self-conjugate nucleus <sup>80</sup>Zr. *Nature Phys.* 589
- 17 (2021) 1408–1412. doi:10.1038/s41567-021-01395-w. 590
- 591 Uberseder E, deBoer RJ. AZURE2 User Manual (2015).
- 592 Foreman-Mackey D, Hogg DW, Lang D, Goodman J. emcee: The MCMC Hammer. Publications of the 593 Astronomical Society of the Pacific 125 (2013) 306–312. doi:10.1086/670067.
- Bahcall JN, Ulrich RK. Solar models, neutrino experiments, and helioseismology. Rev. Mod. Phys. 60 594 (1988) 297-372. doi:10.1103/RevModPhys.60.297. 595
- Cyburt RH, Fields BD, Olive KA, Yeh TH. Big bang nucleosynthesis: Present status. Rev. Mod. Phys. 88 596 (2016) 015004. doi:10.1103/RevModPhys.88.015004. 597
- Kontos A, Uberseder E, deBoer R, Görres J, Akers C, Best A, et al. Astrophysical S factor of  ${}^{3}\text{He}(\alpha,\gamma)^{7}\text{Be}$ . 598 Phys. Rev. C 87 (2013) 065804. doi:10.1103/PhysRevC.87.065804. 599
- Brown TAD, Bordeanu C, Snover KA, Storm DW, Melconian D, Sallaska AL, et al.  ${}^{3}\text{He} + {}^{4}\text{He} \rightarrow {}^{7}\text{Be}$ 600 astrophysical S factor. Phys. Rev. C 76 (2007) 055801. doi:10.1103/PhysRevC.76.055801. 601
- Costantini H, Bemmerer D, Confortola F, Formicola A, Gyürky G, Bezzon P, et al. The  ${}^{3}\text{He}(\alpha,\gamma){}^{7}\text{Be}$ 602
- S-factor at solar energies: The prompt  $\gamma$  experiment at LUNA. Nuclear Physics A 814 (2008) 144–158. 603
- 604 doi:https://doi.org/10.1016/j.nuclphysa.2008.09.014.
- Singh BSN, Hass M, Nir-El Y, Haquin G. New precision measurement of the  ${}^{3}\text{He}({}^{4}\text{He}, \gamma)$   ${}^{7}\text{Be}$  cross 605 section. Phys. Rev. Lett. 93 (2004) 262503. doi:10.1103/PhysRevLett.93.262503. 606
- Carmona-Gallardo M, Nara Singh BS, Borge MJG, Briz JA, Cubero M, Fulton BR, et al. New measurement 607
- of the  ${}^{3}\text{He}(\alpha,\gamma){}^{7}\text{Be}$  cross section at medium energies. Phys. Rev. C 86 (2012) 032801. doi:10.1103/ 608
- 609 PhysRevC.86.032801.
- Bordeanu C, Gyürky G, Halász Z, Szücs T, Kiss G, Elekes Z, et al. Activation measurement of the 610
- $^3$ He( $\alpha, \gamma$ ) $^7$ Be reaction cross section at high energies. *Nuclear Physics A* **908** (2013) 1–11. doi:https: 611
- 612 //doi.org/10.1016/j.nuclphysa.2013.03.012.
- Di Leva A, Gialanella L, Kunz R, Rogalla D, Schürmann D, Strieder F, et al. Stellar and primordial 613
- nucleosynthesis of <sup>7</sup>Be: Measurement of <sup>3</sup>He( $\alpha$ ,  $\gamma$ )<sup>7</sup>Be. *Phys. Rev. Lett.* **102** (2009) 232502. doi:10. 614
- 1103/PhysRevLett.102.232502. 615

- Szücs T, Kiss GG, Gyürky G, Halász Z, Szegedi TN, Fülöp Z. Cross section of  ${}^{3}\text{He}(\alpha, \gamma){}^{7}\text{Be}$  around the <sup>7</sup>Be proton separation threshold. *Phys. Rev. C* **99** (2019) 055804. doi:10.1103/PhysRevC.99.055804. 617
- Adelberger EG, García A, Robertson RGH, Snover KA, Balantekin AB, Heeger K, et al. Solar fusion 618
- cross sections. II. The pp chain and CNO cycles. Rev. Mod. Phys. 83 (2011) 195–245. doi:10.1103/ 619
- RevModPhys.83.195. 620
- Premarathna P, Rupak G. Bayesian analysis of capture reactions  ${}^{3}\text{He}(\alpha, \gamma){}^{7}\text{Be}$  and  ${}^{3}\text{H}(\alpha, \gamma){}^{7}\text{Li}$ . Eur. Jour. 621 Phys. A 56 (2020b) 166. doi:https://doi.org/10.1140/epja/s10050-020-00113-z. 622
- Tursunov E, Turakulov S, Kadyrov A. Analysis of the  ${}^{3}\text{He}(\alpha,\gamma)^{7}\text{Be}$  and  ${}^{3}\text{H}(\alpha,\gamma)^{7}\text{Li}$  astrophysical direct 623
- capture reactions in a modified potential-model approach. Nuclear Physics A 1006 (2021) 122108. 624
- doi:https://doi.org/10.1016/j.nuclphysa.2020.122108. 625
- Nollett KM. Radiative alpha capture cross-sections from realistic nucleon-nucleon interactions and 626
- variational Monte Carlo wave functions. Phys. Rev. C 63 (2001) 054002. doi:10.1103/PhysRevC.63. 627
- 628 054002.
- Neff T. Microscopic calculation of the  ${}^{3}\text{He}(\alpha,\gamma){}^{7}\text{Be}$  and  ${}^{3}\text{H}(\alpha,\gamma){}^{7}\text{Li}$  capture cross sections using realistic 629 interactions. Phys. Rev. Lett. 106 (2011) 042502. doi:10.1103/PhysRevLett.106.042502. 630
- Dohet-Eraly J, Navrátil P, Quaglioni S, Horiuchi W, Hupin G, Raimondi F.  ${}^{3}\text{He}(\alpha, \gamma){}^{7}\text{Be}$  and  ${}^{3}\text{H}(\alpha, \gamma){}^{7}\text{Li}$ 631
- astrophysical S factors from the no-core shell model with continuum. Phys. Lett. B 757 (2016) 430–436. 632
- doi:10.1016/j.physletb.2016.04.021. 633
- Vorabbi M, Navrátil P, Quaglioni S, Hupin G. <sup>7</sup>Be and <sup>7</sup>Li nuclei within the no-core shell model with 634
- continuum. Phys. Rev. C 100 (2019) 024304. doi:10.1103/PhysRevC.100.024304. 635
- Barnard A, Jones C, Weil J. Elastic scattering of 2–11 MeV protons by He<sup>4</sup>. Nuclear Physics **50** (1964) 636
- 604–620. doi:https://doi.org/10.1016/0029-5582(64)90233-0. 637
- Paneru SN, Brune CR, Connolly D, Karpesky J, Davids B, Ruiz C, et al. Elastic scattering of <sup>3</sup>He + <sup>4</sup>He 638
- with SONIK (2022). Unpublished. 639
- deBoer RJ, Görres J, Wiescher M, Azuma RE, Best A, Brune CR, et al. The  $^{12}$ C $(\alpha,\gamma)^{16}$ O reaction and its 640
- implications for stellar helium burning. Rev. Mod. Phys. 89 (2017) 035007. doi:10.1103/RevModPhys. 641
- 89.035007. 642
- Brune CR. Alternative parametrization of R-matrix theory. Phys. Rev. C 66 (2002) 044611. doi:10.1103/ 643
- PhysRevC.66.044611. 644
- Mukhamedzhanov AM, Tribble RE. Connection between asymptotic normalization coefficients, 645
- subthreshold bound states, and resonances. Phys. Rev. C 59 (1999) 3418–3424. doi:10.1103/PhysRevC. 646
- 59.3418. 647
- Mukhamedzhanov AM, Gagliardi CA, Tribble RE. Asymptotic normalization coefficients, spectroscopic 648
- factors, and direct radiative capture rates. Phys. Rev. C 63 (2001) 024612. doi:10.1103/PhysRevC.63. 649
- 024612. 650
- Kiss G, La Cognata M, Spitaleri C, Yarmukhamedov R, Wiedenhöver I, Baby L, et al. Astrophysical 651
- S-factor for the  ${}^{3}\text{He}(\alpha,\gamma)^{7}\text{Be}$  reaction via the asymptotic normalization coefficient (ANC) method. 652
- Physics Letters B 807 (2020) 135606. doi:https://doi.org/10.1016/j.physletb.2020.135606. 653
- Tilley D, Cheves C, Godwin J, Hale G, Hofmann H, Kelley J, et al. Energy levels of light nuclei A = 5, 6, 654
- 7. Nuclear Physics A 708 (2002) 3–163. doi:https://doi.org/10.1016/S0375-9474(02)00597-3. 655
- Paneru SN. Elastic Scattering of <sup>3</sup>He+<sup>4</sup>He with SONIK. Ph.D. thesis, Ohio University (2020). 656
- D'Agostini G. On the use of the covariance matrix to fit correlated data. Nuclear Instruments and Methods
- in Physics Research Section A: Accelerators, Spectrometers, Detectors and Associated Equipment 346 658
- (1994) 306–311. doi:https://doi.org/10.1016/0168-9002(94)90719-6. 659

- 660 Connolly D. Radiative alpha capture on  $S_{34}$  at astrophysically relevant energies and design of a scattering chamber for high precision elastic scattering measurements for the DRAGON experiment. Ph.D. thesis,
- 662 Colorado School of Mines (2015).
- 663 Cyburt RH, Davids B. Evaluation of modern  ${}^{3}\text{He}(\alpha, \gamma){}^{7}\text{Be}$  data. *Phys. Rev. C* **78** (2008) 064614. doi:10.1103/PhysRevC.78.064614.
- 665 Gyürky G, Confortola F, Costantini H, Formicola A, Bemmerer D, Bonetti R, et al.  ${}^{3}\text{He}(\alpha, \gamma)^{7}\text{Be}$  cross section at low energies. *Phys. Rev. C* **75** (2007) 035805. doi:10.1103/PhysRevC.75.035805.
- Confortola F, Bemmerer D, Costantini H, Formicola A, Gyürky G, Bezzon P, et al. Astrophysical s factor of the  ${}^{3}\text{He}(\alpha, \gamma){}^{7}\text{Be}$  reaction measured at low energy via detection of prompt and delayed  $\gamma$  rays. *Phys. Rev. C* **75** (2007) 065803. doi:10.1103/PhysRevC.75.065803.
- Hamilton J, Øverbö I, Tromborg B. Coulomb corrections in non-relativistic scattering. *Nuclear Physics B* 60 (1973) 443–477. doi:https://doi.org/10.1016/0550-3213(73)90193-4.
- van Haeringen H. T matrix and effective range function for coulomb plus rational separable potentials especially for i=1. *Journal of Mathematical Physics* **18** (1977) 927–940. doi:10.1063/1.523373.
- Humblet J. Bessel function expansions of coulomb wave functions. *Journal of Mathematical Physics* **26** (1985) 656–659. doi:10.1063/1.526602.
- 676 Poudel M, Phillips DR. Effective Field Theory analysis of  ${}^{3}\text{He-}\alpha$  scattering data (2021).

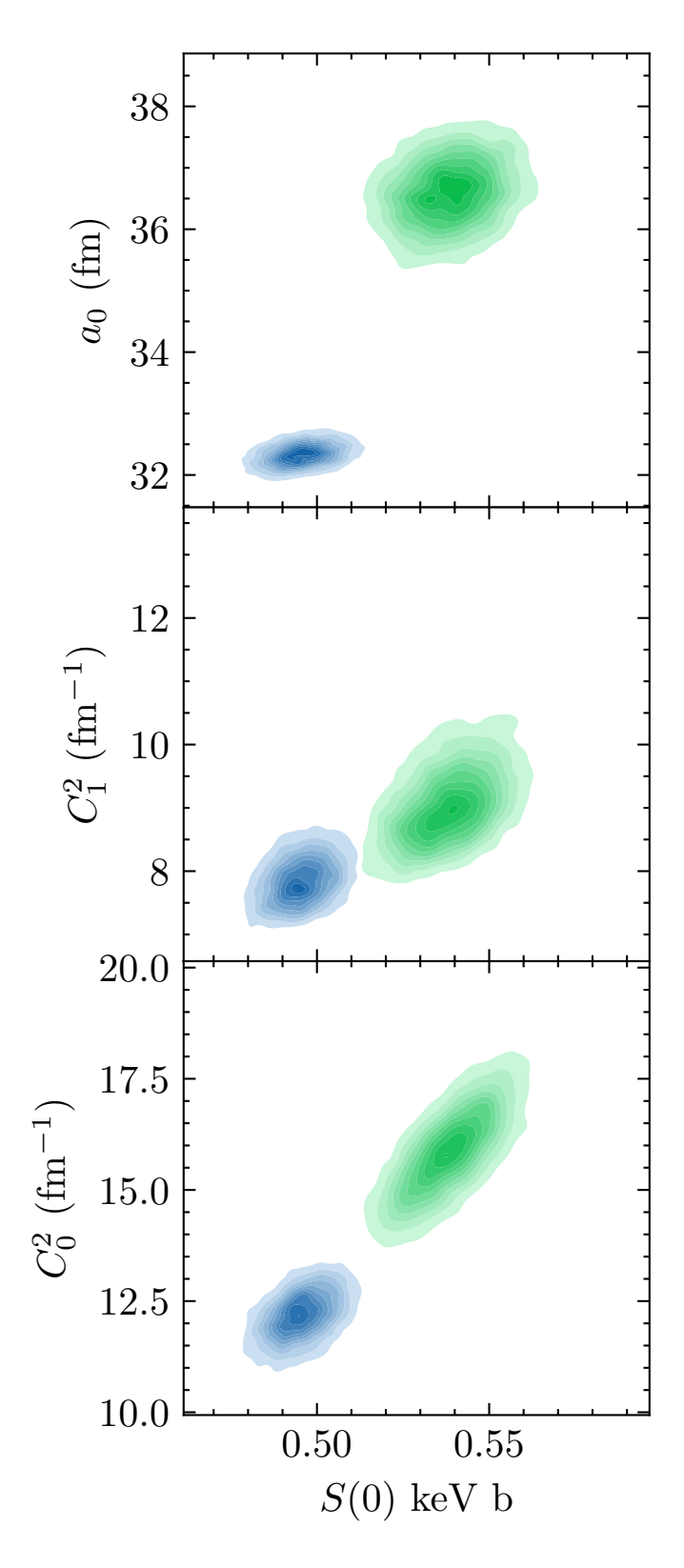


**Figure 16.** Two-dimensional posteriors are presented for the analyses of both  $\mathcal{D}_{\text{CSB}}$  (blue) and  $\mathcal{D}_{\text{CS}}$  (green) data models. The "anchor" parameter is S(0). The top panel gives its correlation with  $a_0$ . The middle (bottom) panel corresponds to the square of the excited- (ground-) state ANC.